The Astrophysical Journal, 738:69 (25pp), 2011 September 1 doi:10.1088/0004-637X/738/1/69
© 2011. The American Astronomical Society. All rights reserved. Printed in the U.S.A.

$z \sim 4$ Hα EMITTERS IN THE GREAT OBSERVATORIES ORIGINS DEEP SURVEY: TRACING THE DOMINANT MODE FOR GROWTH OF GALAXIES

Hyunjin Shim[1], Ranga-Ram Chary[1], Mark Dickinson[2], Lihwai Lin[3], Hyron Spinrad[4], Daniel Stern[5], and Chi-Hung Yan[3]
[1] Spitzer Science Center, California Institute of Technology, MS 220-6, Pasadena, CA 91125, USA
[2] National Optical Astronomy Observatory, 950 North Cherry Avenue, Tucson, AZ 85719, USA
[3] Institute of Astronomy & Astrophysics, Academia Sinica, Taipei 106, Taiwan
[4] Department of Astronomy, University of California at Berkeley, Berkeley, CA 94720, USA
[5] Jet Propulsion Laboratory, California Institute of Technology, Pasadena, CA 91109, USA
Received 2011 March 18; accepted 2011 June 14; published 2011 August 12

ABSTRACT

We present evidence for strong Hα emission in galaxies with spectroscopic redshifts in the range of $3.8 < z < 5.0$ over the Great Observatories Origins Deep Survey fields. Among 74 galaxies detected in the *Spitzer* IRAC 3.6 and 4.5 μm bands, more than 70% of the galaxies show clear excess at 3.6 μm compared to the expected flux density from stellar continuum only. We provide evidence that this 3.6 μm excess is due to Hα emission redshifted into the 3.6 μm band, and classify these 3.6 μm excess galaxies to be Hα emitter (HAE) candidates. The selection of HAE candidates using an excess in broadband filters is sensitive to objects whose rest-frame Hα equivalent width (EW) is larger than 350 Å. The Hα inferred star formation rates (SFRs) of the HAEs range between 20 and 500 $M_\odot$ yr^{-1} and are a factor of ~6 larger than SFRs inferred from the UV continuum. The ratio between the Hα luminosity and UV luminosity of HAEs is also on average larger than that of local starbursts. Possible reasons for such strong Hα emission in these galaxies include different dust extinction properties, young stellar population ages, extended star formation histories, low metallicity, and a top-heavy stellar initial mass function. Although the correlation between UV slope β and $L_{\rm H\alpha}/L_{\rm UV}$ raises the possibility that HAEs prefer a dust extinction curve which is steeper in the UV, the most dominant factor that results in strong Hα emission appears to be star formation history. The Hα EWs of HAEs are large despite their relatively old stellar population ages constrained by spectral energy distribution fitting, suggesting that at least 60% of HAEs produce stars at a constant rate. Under the assumption that the gas supply is sustained, HAEs are able to produce $\gtrsim$50% of the stellar mass density that is encompassed in massive ($M_* > 10^{11}\ M_\odot$) galaxies at $z \sim 3$. This "strong Hα phase" of star formation plays a dominant role in galaxy growth at $z \sim 4$, and they are likely progenitors of massive red galaxies at lower redshifts.

Key words: cosmology: observations – galaxies: evolution – galaxies: high-redshift – galaxies: starburst

Online-only material: color figures

1. INTRODUCTION

Rest-frame near-infrared observations of massive, luminous galaxies at $z \sim 3$ suggest a mode of galaxy growth driven by active star formation at higher redshifts. Despite the discovery of galaxies with extremely large star formation rates (SFRs) such as submillimeter galaxies (SMGs), the number density of observed SMGs significantly drops at $z > 4$ (Schinnerer et al. 2008; Capak et al. 2008; Coppin et al. 2009; Pope & Chary 2010) and is insufficient to explain the number density of massive galaxies at lower redshifts (Coppin et al. 2009). This is either because we miss a significant fraction of $z > 4$ star-forming galaxies or SFR estimates for $z > 4$ galaxies are uncertain. The two possibilities require an understanding of the nature of star formation at high redshifts, especially how the star formation is powered and how well the SFR can be measured.

The dominant mechanism that enables large SFR at high redshifts is unclear. Merger-induced star formation is the preferred mechanism expected in the hierarchical galaxy evolution scenario. Yet the observed number density of galaxies with merger-induced morphologies challenges such a scenario, while the values for merger rates are still a matter of debate (e.g., Ravindranath et al. 2006; Conselice & Arnold 2009). As an alternative way to explain the formation of disks and spheroids at high redshifts, Dekel et al. (2009) suggested a model whereby accretion of cold gas along dark matter filaments powers star formation in galaxies. Although no direct evidence for cold gas accretion has been observed that supports this scenario, the effect of cold stream feeding into massive dark matter halos increases at $z > 2$. Thus, the expected number density of galaxies at $z > 2$ with large SFR would be larger than the number density of merger-powered star-forming galaxies at high redshifts. In order to assess whether merger or accretion is the main mechanism for growth of stellar mass in galaxies, large samples of galaxies with well-measured SFRs are necessary.

The most popular probe of star formation history at high redshift is the rest-frame UV emission due to the practical reason that the rest-frame UV is redshifted to optical wavelengths and easily accessible at $z > 3$. The Lyman break galaxies (LBGs; Steidel et al. 2003; Ouchi et al. 2004; Bouwens et al. 2007, 2009, 2010) selected using rest-frame UV colors and the Lyman alpha emitters (LAEs; Malhotra & Rhoads 2002; Shioya et al. 2009; Taniguchi et al. 2009) selected in narrowband and grism observations are the best tracers of the star-forming galaxy population at $z > 3$. Despite their wide usage, it is not clear whether these UV-selected galaxy samples and UV-inferred SFRs account for most of the ongoing star formation, since the UV emission is by nature, sensitive to dust extinction (Bouwens et al. 2009).

While high-redshift star-forming galaxies do show evidence for dust attenuation (e.g., Adelberger & Steidel 2000; Reddy et al. 2010), a precise understanding of their internal reddening

properties is missing. The UV spectral slope β ($f_\lambda \propto \lambda^\beta$) has been widely used for extinction correction, using its tight correlation with other extinction measures in the local universe (Meurer et al. 1999). Several studies have tested its validity at higher redshifts up to $z \sim 2$ (Papovich et al. 2006; Daddi et al. 2007; Reddy et al. 2010), yet the studies for star-forming galaxies at even higher redshifts suggest that this is not true: for example, Siana et al. (2009) show that it may not be valid to use the extinction law for local starbursts (Calzetti et al. 2000) for young LBGs at $z \sim 3$, since the UV slope β overpredicts the level of dust extinction. Carilli et al. (2008) demonstrated that radio-derived SFRs for $z \sim 3$ LBGs indicate UV extinction smaller than estimated before. Hayes et al. (2010) claimed that the extinction in LAEs should be larger than that suggested by the starburst extinction law (Calzetti et al. 2000). These recent studies suggest that the dust extinction properties of high-redshift star-forming galaxies could be different from that of the local galaxies.

This potential difference in dust extinction of high-redshift star-forming galaxies compared to local starbursts is constrained through the comparison of UV-inferred star formation to the star formation from other independent indicators that are less sensitive to the dust extinction (e.g., Reddy et al. 2010). The optical emission lines, especially the Balmer recombination lines, enable a direct comparison between local starbursts and high-redshift star-forming galaxies. Moreover, these lines are less sensitive to dust extinction compared to UV emission lines or continuum measurements. However, it is not easy to investigate optical emission lines of high-redshift star-forming galaxies through spectroscopic observations when the lines are redshifted to the near-infrared. It is impossible to measure Hα line flux at $z > 4$ ($>3\,\mu$m) with current facilities, although there are studies measuring Hα line flux for $z \sim 2$ galaxies through NIR spectroscopy (Erb et al. 2006; Reddy et al. 2010) or narrowband imaging (Geach et al. 2008; Hayes et al. 2010).

In order to overcome these observational limits, we propose to use photometric information from high-redshift star-forming galaxies that reflect the presence of the line emission when the line is sufficiently strong. Chary et al. (2005) have constrained SFR of a $z = 6.56$ lensed galaxy using the observed increase in *Spitzer* 4.5 μm flux which is likely to be due to Hα emission. Other studies of the spectral energy distributions (SEDs) of high-redshift star-forming galaxies have also suggested that strong emission lines affect the broadband photometry (Schaerer et al. 2009; Reddy et al. 2010). Unbiased surveys for emission-line galaxies (e.g., WFC3 grism surveys, Atek et al. 2010) showed that there do exist galaxies with very faint continuum but strong Hα emission line at $z \sim 1$–2. Such galaxies could be selected using the existing NIR/MIR photometric observations in the appropriate redshift window. This paper is focused on the identification and investigation of such galaxies with strong rest-frame optical emission lines.

In this paper, we present the SFRs of $z \sim 4$ galaxies measured using the Hα line. This is the first rest-frame optical estimation of SFRs for spectroscopically confirmed $z \sim 4$ galaxies. The Hα line flux is estimated through an excess in the broadband (i.e., *Spitzer* 3.6 μm) photometry over the stellar continuum. By comparing the stellar population model parameters derived by fitting the multiwavelength photometry with population synthesis models and Hα SFRs, we address several critical issues of star formation at $z \sim 4$: (1) whether the dust extinction corrections applied for local starbursts are still valid at $z \gtrsim 4$, (2) how star-forming galaxies at $z \gtrsim 4$ are related to massive galaxies at lower redshifts, and (3) whether mergers or stream-fed accretion is the dominant process that powers the star formation at $z \gtrsim 4$. Throughout this paper, we use a cosmology with $\Omega_M = 0.27$, $\Omega_\Lambda = 0.73$, and $H_0 = 71\,\mathrm{km\,s^{-1}\,Mpc^{-1}}$.

2. SAMPLE

2.1. $3.8 < z_{\rm spec} < 5.0$ Galaxies in GOODS

From the various spectroscopic observing programs over the Great Observatories Origins Deep Survey (GOODS) North and South field (including Vanzella et al. 2005, 2006, 2008; Ando et al. 2004), we select galaxies with secure spectroscopic redshifts between $z = 3.8$ and 5.0. The redshift window of $3.8 < z < 5.0$ is chosen to select galaxies whose redshifted Hα emission line enters into the *Spitzer* IRAC channel 1 (ch1) (3.6 μm) band (Figure 1 (top); see Section 3 for details). Provided that the signal-to-noise (S/N) ratios in IRAC ch1 and channel 2 (ch2) (4.5 μm) images are high enough, the underlying stellar continuum and hence the level of possible ch1 excess due to the Hα emission line are accurately derived in these galaxies through SED fitting. The IRAC ch1 photometry point is excluded in the SED fitting. Furthermore, in this redshift range, strong emission lines other than Hα—e.g., Hβ, [O III]—do not affect the fluxes in other filters since these lines fall in the gap between the IRAC ch1 and K band. The [O II] $\lambda\lambda$3727 emission line does fall in the K band at $z > 4.4$, yet it would not affect the determination of the stellar continuum. We estimated the excess in K-band photometry due to the [O II] emission line, considering the ratio between [O II] and the Hα line (Mouhcine et al. 2005) and the estimated Hα luminosity for $z \sim 4$ galaxies in our sample. The excess in K-band photometry due to the existing [O II] line over the stellar continuum is at most 10%. This is much smaller than the case of IRAC ch1, where the excess in the flux density is larger than 30% (see Section 3 for details). This is mainly due to the difference in equivalent widths (EWs) for [O II] and Hα, where [O II] EWs are in general less than 50 Å while Hα EWs are even larger than 100 Å for actively star-forming galaxies.

Over the total area of 330 arcmin^2 of the GOODS-North (centered on $12^{\rm h}36^{\rm m}49^{\rm s}.4$, $62^\circ12'58''.0$) and the GOODS-South ($3^{\rm h}32^{\rm m}28^{\rm s}.0$, $-27^\circ48'30''.0$), the initial number of galaxies with reliable spectroscopic redshifts of $3.8 < z < 5.0$ is 124: 53 galaxies in the GOODS-North field and 71 galaxies in the GOODS-South field. The surveyed comoving volume at this redshift range is 1.2×10^6 Mpc^3. Among these galaxies, we apply an S/N cut for IRAC ch1 and ch2 band ($\mathrm{S/N}_{3.6\,\mu\mathrm{m}}$, $\mathrm{S/N}_{4.5\,\mu\mathrm{m}} > 5$) to guarantee the accurate determination of underlying stellar continuum. We also apply an isolation criteria, removing galaxies with close neighbors (z-band magnitude brighter than $m + 2$, when m is the magnitude of the galaxy in consideration) within 1″ from the final sample. This is to ensure that their *Spitzer*/IRAC photometry is not contaminated by neighboring galaxies due to the fact that the point-spread function of *Spitzer*/IRAC images is 1″.5 in channels 1 and 2, and 1″.8–2″.0 in channel 3 (ch3) and channel 4 (ch4), respectively. The value of 1″ is less than the true FWHM in IRAC images, which is ∼2″. If we restrict the allowed radius for neighbors to be 2″ to match with the FWHM, ∼25% of galaxies would be thrown out from the sample. The postage stamp images for sample galaxies are presented later in Section 5.1 (Figures 9 and 10). In the end, we are left with 31 (GOODS-North) and 43 (GOODS-South) isolated galaxies at $3.8 < z < 5.0$.

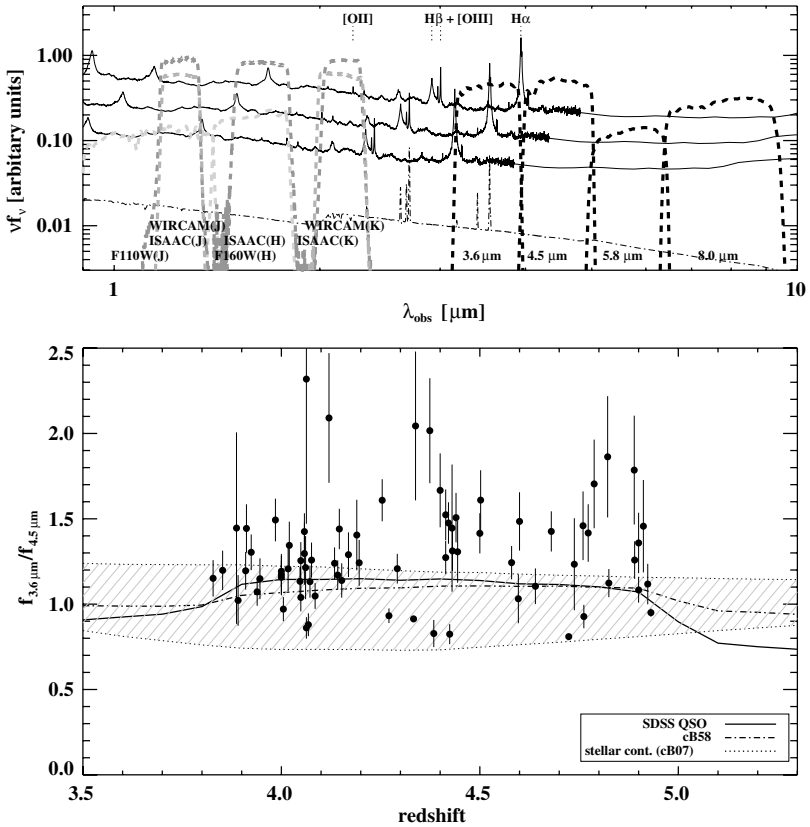

Figure 1. Top: the expected spectra of objects with emission lines at $3.8 < z < 5.0$. The solid lines indicate the spectrum of the Sloan Digital Sky Survey composite quasar (Vanden Berk et al. 2001), redshifted to $z = 3.8$, 4.4, and 5.0, respectively (from bottom to top). The dot-dashed line is the spectrum of the $z = 2.73$ star-forming galaxy MS1512-cB58 (Teplitz et al. 2004) redshifted to $z = 4.4$. The Hα emission line enters IRAC ch1 (3.6 μm band) at $z \sim 3.8$ and exits ch1 at $z \sim 5.0$. Bottom: the change of the flux ratio $f_{3.6\,\mu\mathrm{m}}/f_{4.5\,\mu\mathrm{m}}$ as a function of redshift. The solid line and dot-dashed line indicate $f_{3.6\,\mu\mathrm{m}}/f_{4.5\,\mu\mathrm{m}}$ for the redshifted SDSS quasar and cB58, respectively. As the Hα emission line enters IRAC ch1, the ratio $f_{3.6\,\mu\mathrm{m}}/f_{4.5\,\mu\mathrm{m}}$ increases at $3.8 < z < 5.0$. The dotted lines and the hatched region indicate the range of $f_{3.6\,\mu\mathrm{m}}/f_{4.5\,\mu\mathrm{m}}$ spanned by stellar population synthesis model templates (CB07; Bruzual 2007) which are constrained by the rest-frame UV to optical SEDs of the spectroscopically selected $3.8 < z < 5.0$ galaxies studied in this paper. The observed $f_{3.6\,\mu\mathrm{m}}/f_{4.5\,\mu\mathrm{m}}$ values of our sample of galaxies at $3.8 < z < 5.0$ are overplotted as filled circles with error bars. A flux density excess at 3.6 μm is clearly evident. We use full SED fits to the multiwavelength photometry to measure the exact contribution of line emission to the broadband photometry.

2.2. Optical to Mid-infrared Photometry

In this study, we used the optical-to-MIR merged photometric catalog over GOODS-South and GOODS-North to obtain multi-band photometric data for those objects with spectroscopic redshifts in the range of $3.8 < z < 5.0$.

The optical bands included are the *Hubble Space Telescope*/Advanced Camera for Surveys (*HST*/ACS) F435W, F606W, F775W, and F850LP (generally referred to as B, V, i, and z) bands (Giavalisco et al. 2004). For optical photometry, sources were detected in z-band images, and photometry was carried out through matched apertures in other ACS bands using SExtractor (Bertin & Arnouts 1996). The range of z-band magnitudes is 23.5–26.5 mag. Most $3.8 < z < 5.0$ galaxies are clear B-dropouts with non-detections in B band. In the *Spitzer*/IRAC images of GOODS[6] (Dickinson et al. 2003), the flux densities are measured using 4″ diameter apertures with aperture corrections applied afterward. In order to check whether the high confusion in IRAC bands matters in the photometry, we compared this "aperture" photometry with the result of "Template Fitting" (TFIT) photometry (Laidler et al. 2007), which is obtained using the matched apertures defined in the z band. For bright galaxies (S/N $>$ 10 in 3.6 μm and 4.5 μm), there are no systematic differences between the aperture photometry and TFIT photometry. On the other hand, TFIT results in higher flux measurements compared to aperture photometry for low S/N galaxies since it applies a larger correction factor to account for the contribution from outskirts of galaxies that are below the noise threshold in the *Spitzer* images. Since we adopted a high S/N cut in sample selection and constrained the sample to be relatively isolated (Section 2.1), the photometric uncertainties in the IRAC bands due to source confusion are small. Nevertheless, we included the systematic uncertainties in IRAC fluxes based on the difference between the aperture and TFIT photometry in the estimation of flux errors by adding the square of the systematic uncertainties to the photometric uncertainties. For IRAC ch3 and 4, if the source is undetected, we use the 3σ upper limit to the flux density in the 4″ aperture at the location of the sources.

NIR photometry is important for these galaxies since the Balmer break, which is a critical constraint on the age of the stellar population, falls between the K and the *Spitzer*/IRAC 3.6 μm bands. We derived the NIR photometry of sample galaxies by matching the sample catalog with the available data from NIR observing programs. When available, we used *HST*/NICMOS J_{110} and H_{160} fluxes (Conselice et al. 2011; Dickinson 1999). For galaxies in GOODS-South, we used Very Large Telescope (VLT)/ISAAC J-/H-/K-band photometry of galaxies (Retzlaff et al. 2010). More than 90% of the

[6] The *Spitzer*/IRAC observation on GOODS have been obtained as a part of the *Spitzer* Legacy program. The details of the observation and the data description is on the *Spitzer* Legacy website.

$3.8 < z < 5.0$ galaxies have counterparts in NIR source catalogs. The NIR observations in GOODS-North were carried out with Wide-Field Near Infrared Camera (WIRCAM) on the Canada–France–Hawaii Telescope (CFHT) during the years 2006–2009. This includes 27.4 hr of integration in J band made by a Taiwanese group and 31.9 hr of integration in K_s band obtained by Hawaiian and Canadian observing programs. The WIRCAM K_s-band data have recently been published by Wang et al. (2010), but here we use our own version of the reductions (L. Lin et al. 2011, in preparation). The data were first pre-processed using the SIMPLE Imaging and Mosaicking Pipeline (Wang et al. 2010) and then combined to produce deep stacks with Software for Calibrating AstroMetry and Photometry (SCAMP; Bertin 2006) and SWARP (Bertin et al. 2002).[7] The resulting 5σ limiting magnitudes using $2''$ diameter circular apertures reach $J = 24.8$ mag(AB) and $K_s = 24.35$ mag(AB). For galaxies with non-detections in the NIR, we provide 3σ flux density upper limits in the $4''$ aperture measured in the corresponding images.

The multi-band photometry for the 74 galaxies at $3.8 < z < 5.0$ considered here, including upper limits when needed, is presented in Table 1.

3. Hα EMITTER IDENTIFICATION

The basic assumption in this photometric study of the Hα emission in $z \sim 4$ galaxies is that the redshifted Hα emission line causes an enhancement in the broadband flux density. Specifically, the Hα emission line is redshifted into the *Spitzer*/IRAC ch1 band at $3.8 < z < 5.0$. We define such galaxies with a large rest-frame Hα EW that yields an excess in IRAC ch1 photometry compared to the stellar continuum as "Hα emitters (hereafter HAEs)." In this section, we show that the observed photometric excess is due to the redshifted Hα emission and describe the procedure used to derive the Hα line luminosity and EW of HAEs.

3.1. IRAC Color

The amount of excess in the *Spitzer*/IRAC ch1 band reaches ∼10% if the galaxy observed at $3.8 < z < 5.0$ is a star-forming galaxy with Hα EW of 100 Å (Figure 1 (top)). This is illustrated in Figure 1 (bottom), where the expected $f_{3.6\,\mu\mathrm{m}}/f_{4.5\,\mu\mathrm{m}}$ ratio of model galaxy templates are plotted as a function of redshift. The dot-dashed line is the expected $f_{3.6\,\mu\mathrm{m}}/f_{4.5\,\mu\mathrm{m}}$ ratio calculated using the template of star-forming galaxy MS1512-cB58 with $\mathrm{EW}_{\mathrm{H}\alpha} = 100$ Å. The $f_{3.6\,\mu\mathrm{m}}/f_{4.5\,\mu\mathrm{m}}$ ratio increases significantly at $3.8 < z < 5.0$, where the Hα line is redshifted into $3.6\,\mu$m band. The Sloan quasar template (solid line) shows a similar trend as the star-forming galaxy.

Figure 1 (bottom) also reveals if the increase in $f_{3.6\,\mu\mathrm{m}}/f_{4.5\,\mu\mathrm{m}}$ can be explained using changes to the properties of the stellar population only, by showing the bluest and the reddest $f_{3.6\,\mu\mathrm{m}}/f_{4.5\,\mu\mathrm{m}}$ colors possible from the stellar continuum for the Charlot & Bruzual 2007 (hereafter CB07; Bruzual 2007) population synthesis model spanning a range of starburst age, star formation history, and dust extinction. The range of parameters used in stellar population synthesis model is constrained by the rest-frame UV to optical colors of our sample galaxies: ages between 3 Myr and ∼1000 Myr old, $E(B-V)$ between 0.0 and ∼0.4. The overplotted data points in Figure 1 (bottom) are the observed $f_{3.6\,\mu\mathrm{m}}/f_{4.5\,\mu\mathrm{m}}$ ratio for our sample galaxies at $3.8 < z < 5.0$. Among 74 galaxies, 63 sources show $f_{3.6\,\mu\mathrm{m}}/f_{4.5\,\mu\mathrm{m}}$ ratios larger than 1 and 58 sources show $f_{3.6\,\mu\mathrm{m}}/f_{4.5\,\mu\mathrm{m}}$ ratios larger (i.e., bluer ch1−ch2 color) than that of MS1512-cB58. The large $f_{3.6\,\mu\mathrm{m}}/f_{4.5\,\mu\mathrm{m}}$ ratios that are observed could be produced in many cases using younger stellar populations and less dust extinction. Yet, when the measured broadband flux is larger than ∼50%–150% of the expected stellar continuum (e.g., Chary et al. 2005; Zackrisson et al. 2008), it is impossible to reproduce the observed excess by changing the stellar continuum only. This requires the inclusion of strong emission lines to fully explain the observed broadband photometry excess. We fit the SED of each galaxy to constrain the age of the stellar population and dust extinction and, in addition, measure the contribution of the Hα emission line to the broadband flux density.

3.2. Spectral Energy Distribution Fitting

Although the blue IRAC color (high $f_{3.6\,\mu\mathrm{m}}/f_{4.5\,\mu\mathrm{m}}$) is a sign that suggests the presence of strong Hα emission in these galaxies, the color alone is insufficient to identify HAEs since the effect of stellar population age and dust extinction to the broadband color is not constrained. In order to determine the underlying stellar continuum in IRAC ch1 and to disentangle the relative contributions from stellar radiation and from line emission to the ch1-band flux, we fit the multi-band photometry of all $3.8 < z < 5.0$ galaxies using the CB07 stellar population synthesis model.

We used the galaxy models of fixed metallicity $0.2\,Z_\odot$, considering the relatively low metallicity of high-redshift star-forming galaxies (e.g., Pettini et al. 2002). Salpeter initial mass function (IMF; Salpeter 1955) is used to generate galaxy templates. Star formation histories of the model galaxies are varied using different values for the exponentially decaying star formation timescale, i.e., $\tau = [1, 10, 20, 30, 40, 50, 60, 70, 80, 90, 100, 200, 300, 400, 500, 600, 700, 800, 900, 1000]$ Myr and $\tau = 10^5$ Myr (constant star formation). The ages of model galaxies are varied to span the range between 1 Myr and the age of the universe at the given redshift. For internal reddening of the model galaxy templates, we used two forms of extinction law: the extinction law for local starbursts (SB; Calzetti et al. 2000) and the extinction law for the Small Magellanic Cloud (SMC; Prévot et al. 1984). The SMC extinction law is expected to describe low-metallicity galaxies well, which results in more rapidly increasing extinction with decreasing wavelength in the UV. The internal dust extinction is allowed to vary between $E(B-V) = 0$ and $E(B-V) = 0.6$ for both extinction laws. The best-fit template is determined through χ^2 minimization where χ^2 is defined as follows:

$$\chi^2 = \sum_{\mathrm{filter}} \frac{(f_{\mathrm{obs}} - f_{\mathrm{mod}})^2}{\sigma_{\mathrm{obs}}^2}. \quad (1)$$

The model flux f_{mod} is calculated by convolving the filter response curve to the galaxy template, after applying the intergalactic medium attenuation (Madau 1995).

Because we wish to evaluate any potential flux excess in *Spitzer*/IRAC ch1 ($3.6\,\mu$m) from an emission line, we initially exclude the ch1 photometry in the SED fitting. The photometry data points used in the fits are *HST*/ACS B-, V-, i-, and z-band flux, NIR flux (*HST*/NICMOS F110W and F160W when available; VLT/ISAAC J, H, and K bands for GOODS-South; CFHT/WIRCAM J and K bands for GOODS-North) and *Spitzer*/IRAC ch2, ch3 ($5.8\,\mu$m), and ch4 ($8.0\,\mu$m) flux.

[7] http://www.astromatic.net/

Table 1
Photometry of Galaxies at $3.8 < z < 5.0$

ID	R.A.	Decl.	$z_{\rm spec}$	B	V	i	z	F110W	F160W	J	H	K	3.6 μm	4.5 μm	5.8 μm	8.0 μm
S1213	3 32 04.06	−27 43 22.77	4.017	>28.9	26.12 ± 0.15	25.43 ± 0.13	25.15 ± 0.12	...	...	24.85 ± 0.13	24.71 ± 0.15	23.91 ± 0.08	23.75 ± 0.07	23.95 ± 0.10	24.51 ± 0.86	>22.54
S1461	3 32 05.02	−27 46 12.65	3.912	27.67 ± 0.29	25.16 ± 0.06	24.54 ± 0.06	24.47 ± 0.06	...	...	24.56 ± 0.07	24.64 ± 0.16	24.46 ± 0.14	23.27 ± 0.06	23.67 ± 0.09	22.81 ± 0.20	24.08 ± 0.68
S1478	3 32 05.08	−27 46 56.52	4.825	30.21 ± 3.67	26.22 ± 0.13	23.97 ± 0.06	23.79 ± 0.06	...	24.09 ± 0.11	...	...	...	22.00 ± 0.06	22.13 ± 0.06	21.82 ± 0.10	22.11 ± 0.14
S1944	3 32 06.61	−27 47 47.70	3.939	28.53 ± 0.71	25.08 ± 0.07	24.40 ± 0.06	24.28 ± 0.06	...	...	...	...	...	22.71 ± 0.06	22.79 ± 0.06	23.16 ± 0.25	22.60 ± 0.17
S4142	3 32 11.71	−27 41 49.59	4.912	28.90 ± 0.70	27.27 ± 0.16	25.55 ± 0.07	25.36 ± 0.07	...	...	25.35 ± 0.08	25.28 ± 0.10	24.94 ± 0.12	24.44 ± 0.09	24.85 ± 0.18	>22.39	>22.54
S4168	3 32 11.78	−27 51 08.25	3.828	29.14 ± 1.00	26.01 ± 0.07	25.38 ± 0.07	25.19 ± 0.07	...	...	25.16 ± 0.12	25.15 ± 0.22	24.70 ± 0.14	23.56 ± 0.06	23.71 ± 0.08	>22.39	>22.54
S4773	3 32 12.99	−27 48 33.75	4.292	>28.9	26.74 ± 0.12	25.62 ± 0.09	25.43 ± 0.08	...	...	26.12 ± 0.55	25.06 ± 0.34	24.83 ± 0.29	23.97 ± 0.03	24.18 ± 0.07	>22.39	>22.54
S5533	3 32 14.50	−27 49 32.68	4.738	30.65 ± 5.50	26.39 ± 0.11	25.51 ± 0.09	25.40 ± 0.09	...	25.68 ± 0.21	25.16 ± 0.10	25.92 ± 0.36	25.71 ± 0.30	25.19 ± 0.11	25.41 ± 0.21	24.73 ± 0.68	>22.54
S6665	3 32 16.64	−27 42 53.35	3.891	27.03 ± 0.18	25.27 ± 0.06	24.86 ± 0.06	24.81 ± 0.06	...	...	24.60 ± 0.05	24.45 ± 0.05	25.55 ± 0.23	24.44 ± 0.09	24.46 ± 0.13	23.86 ± 0.43	>22.54
S6854	3 32 16.98	−27 51 23.17	4.600	>28.9	27.27 ± 0.24	25.29 ± 0.08	25.30 ± 0.09	...	24.77 ± 0.15	25.30 ± 0.15	24.37 ± 0.10	24.37 ± 0.11	23.84 ± 0.07	24.27 ± 0.11	>22.39	>22.54
S6867	3 32 17.00	−27 41 13.72	4.414	28.90 ± 0.90	26.66 ± 0.13	25.30 ± 0.07	25.09 ± 0.07	...	...	24.73 ± 0.07	24.43 ± 0.07	24.31 ± 0.10	23.37 ± 0.06	23.83 ± 0.09	23.56 ± 0.34	23.44 ± 0.32
S8067	3 32 19.02	−27 52 38.15	4.431	27.82 ± 0.74	25.51 ± 0.10	24.38 ± 0.07	24.27 ± 0.07	...	...	24.17 ± 0.05	24.30 ± 0.09	23.64 ± 0.05	23.36 ± 0.06	23.66 ± 0.07	23.72 ± 0.36	23.84 ± 0.43
S8787	3 32 20.29	−27 47 18.18	4.254	27.54 ± 0.26	25.70 ± 0.07	24.29 ± 0.06	23.96 ± 0.05	...	...	23.35 ± 0.02	23.16 ± 0.02	23.08 ± 0.03	22.72 ± 0.06	23.24 ± 0.06	>22.39	>22.54
S9738	3 32 21.93	−27 45 33.08	4.788	>28.9	28.15 ± 0.45	26.59 ± 0.19	25.82 ± 0.12	...	25.44 ± 0.20	25.99 ± 0.22	25.01 ± 0.14	24.59 ± 0.08	24.09 ± 0.07	24.67 ± 0.15	>22.39	>22.54
S10232	3 32 22.71	−27 51 54.38	4.900	30.65 ± 6.50	27.54 ± 0.37	25.81 ± 0.13	25.54 ± 0.12	...	...	25.25 ± 0.11	27.27 ± 1.21	24.83 ± 0.13	24.09 ± 0.08	24.42 ± 0.12	24.16 ± 0.53	>22.54
S10340	3 32 22.88	−27 47 27.57	4.440	>28.9	26.68 ± 0.12	25.03 ± 0.07	24.93 ± 0.06	...	...	24.66 ± 0.06	24.72 ± 0.09	24.53 ± 0.36	23.69 ± 0.06	24.14 ± 0.09	23.73 ± 0.28	24.42 ± 0.59
S10388	3 32 22.97	−27 46 29.09	4.500	28.62 ± 1.08	27.45 ± 0.34	25.66 ± 0.12	25.33 ± 0.10	...	...	24.57 ± 0.07	24.34 ± 0.09	23.86 ± 0.31	23.10 ± 0.06	23.48 ± 0.07	23.40 ± 0.24	23.65 ± 0.35
S12424	3 32 26.18	−27 52 11.28	4.068	29.01 ± 1.67	25.04 ± 0.07	24.45 ± 0.06	24.37 ± 0.07	...	...	24.21 ± 0.17	23.66 ± 0.05	23.76 ± 0.05	23.01 ± 0.06	22.88 ± 0.06	22.91 ± 0.18	22.74 ± 0.16
S12652	3 32 26.49	−27 41 23.97	4.384	27.29 ± 0.32	25.51 ± 0.07	24.93 ± 0.07	24.96 ± 0.08	...	...	25.44 ± 0.16	24.87 ± 0.15	24.04 ± 0.13	23.89 ± 0.07	23.68 ± 0.08	24.62 ± 0.86	>22.54
S13025	3 32 27.01	−27 41 28.02	4.333	>28.9	27.42 ± 0.26	26.44 ± 0.19	25.68 ± 0.11	...	...	23.91 ± 0.06	23.05 ± 0.04	22.10 ± 0.03	21.09 ± 0.01	20.99 ± 0.02	21.16 ± 0.14	21.39 ± 0.23
S13297	3 32 27.37	−27 55 27.37	4.271	29.29 ± 1.57	26.43 ± 0.11	25.32 ± 0.08	25.15 ± 0.08	...	25.05 ± 0.17	25.55 ± 0.18	24.69 ± 0.08	25.18 ± 0.17	23.29 ± 0.03	23.21 ± 0.04	22.81 ± 0.20	22.84 ± 0.24
S13701	3 32 27.94	−27 46 18.56	4.000	>28.9	26.31 ± 0.08	25.28 ± 0.07	25.23 ± 0.07	...	...	24.76 ± 0.08	24.84 ± 0.12	24.18 ± 0.05	23.96 ± 0.06	24.14 ± 0.09	23.77 ± 0.32	23.92 ± 0.42
S14097	3 32 28.56	−27 40 55.72	4.597	>28.9	27.32 ± 0.21	25.48 ± 0.08	25.44 ± 0.08	...	...	25.33 ± 0.15	...	25.69 ± 0.40	24.36 ± 0.08	24.39 ± 0.13	24.11 ± 0.56	26.01 ± 3.43
S14602	3 32 29.29	−27 56 19.46	4.762	>28.9	26.83 ± 0.10	25.21 ± 0.06	25.05 ± 0.06	...	...	...	...	...	22.56 ± 0.06	22.47 ± 0.06	21.81 ± 0.09	21.30 ± 0.07
S15920	3 32 31.19	−27 54 29.33	4.005	28.32 ± 0.59	27.03 ± 0.18	26.42 ± 0.16	25.82 ± 0.11	...	23.29 ± 0.10	23.82 ± 0.03	22.78 ± 0.01	22.43 ± 0.01	22.31 ± 0.06	22.28 ± 0.06	22.15 ± 0.10	22.81 ± 0.18
S17126	3 32 33.03	−27 47 59.63	4.063	27.37 ± 0.41	26.22 ± 0.14	25.66 ± 0.14	25.33 ± 0.11	...	...	24.45 ± 0.18	23.88 ± 0.18	23.19 ± 0.09	22.89 ± 0.06	22.73 ± 0.06	22.66 ± 0.11	22.48 ± 0.10
S17403	3 32 33.47	−27 50 30.00	4.900	>28.9	28.20 ± 0.37	26.47 ± 0.14	25.76 ± 0.09	...	...	25.51 ± 0.09	25.20 ± 0.12	24.79 ± 0.07	23.69 ± 0.04	23.78 ± 0.06	23.72 ± 0.38	23.88 ± 0.56
S17579	3 32 33.77	−27 52 23.70	4.724	>28.9	26.19 ± 0.11	25.34 ± 0.09	25.25 ± 0.09	...	...	24.78 ± 0.06	23.79 ± 0.05	23.30 ± 0.03	22.20 ± 0.01	21.97 ± 0.01	21.80 ± 0.08	21.71 ± 0.08
S17728	3 32 33.98	−27 48 02.03	4.640	>28.9	27.29 ± 0.18	26.08 ± 0.11	25.84 ± 0.10	...	...	25.70 ± 0.13	25.46 ± 0.18	24.22 ± 0.19	24.04 ± 0.06	24.15 ± 0.08	>22.39	>22.54
S17994	3 32 34.35	−27 48 55.79	4.142	28.62 ± 1.54	25.17 ± 0.08	24.27 ± 0.07	24.11 ± 0.07	...	...	24.05 ± 0.03	23.90 ± 0.05	23.33 ± 0.03	22.83 ± 0.06	23.00 ± 0.06	22.89 ± 0.13	>22.54
S20830	3 32 38.73	−27 44 13.34	4.000	>28.9	26.03 ± 0.14	25.04 ± 0.10	24.81 ± 0.09	...	...	24.26 ± 0.09	24.15 ± 0.17	23.32 ± 0.08	23.28 ± 0.06	23.44 ± 0.07	23.46 ± 0.28	23.29 ± 0.27
S21686	3 32 40.12	−27 45 35.49	4.773	29.65 ± 1.80	27.34 ± 0.21	25.63 ± 0.09	25.54 ± 0.09	...	...	25.03 ± 0.06	25.09 ± 0.13	25.48 ± 0.20	23.96 ± 0.07	24.34 ± 0.11	>22.39	>22.54
S21819	3 32 40.38	−27 44 31.01	4.120	29.01 ± 0.89	25.74 ± 0.07	25.24 ± 0.07	25.24 ± 0.07	...	...	25.38 ± 0.06	25.06 ± 0.09	24.91 ± 0.09	24.10 ± 0.07	24.91 ± 0.18	24.52 ± 0.75	>22.54
S22255	3 32 41.16	−27 51 01.46	4.058	>28.9	25.92 ± 0.09	25.31 ± 0.09	25.25 ± 0.09	...	...	24.98 ± 0.09	25.80 ± 0.92	24.71 ± 0.44	24.30 ± 0.08	24.58 ± 0.13	>22.39	>22.54
S22746	3 32 42.05	−27 47 40.58	4.049	27.64 ± 0.38	25.86 ± 0.08	25.47 ± 0.09	25.47 ± 0.10	...	...	24.96 ± 0.07	23.93 ± 0.05	23.60 ± 0.04	23.40 ± 0.06	23.44 ± 0.06	23.56 ± 0.24	23.28 ± 0.20
S23040	3 32 42.62	−27 54 28.95	4.400	29.89 ± 2.75	27.67 ± 0.32	25.75 ± 0.10	25.62 ± 0.10	...	...	25.46 ± 0.14	25.24 ± 0.10	24.50 ± 0.09	23.89 ± 0.07	24.44 ± 0.12	>22.39	>22.54
S23745	3 32 44.07	−27 42 27.43	4.923	>28.9	27.11 ± 0.25	25.01 ± 0.08	24.98 ± 0.08	...	24.90 ± 0.16	25.02 ± 0.08	25.02 ± 0.19	24.79 ± 0.15	23.76 ± 0.07	23.88 ± 0.09	>22.39	>22.54
S23763	3 32 44.11	−27 54 52.53	4.931	26.29 ± 0.20	24.78 ± 0.07	24.41 ± 0.07	24.50 ± 0.08	...	...	24.50 ± 0.08	23.47 ± 0.03	23.19 ± 0.04	22.36 ± 0.02	22.31 ± 0.02	22.35 ± 0.16	22.21 ± 0.16
S24739	3 32 46.25	−27 48 46.98	4.020	>28.9	25.65 ± 0.06	24.89 ± 0.06	24.88 ± 0.06	...	...	24.79 ± 0.06	24.96 ± 0.14	24.31 ± 0.08	23.93 ± 0.06	24.25 ± 0.09	23.62 ± 0.26	24.04 ± 0.43
S25586	3 32 48.24	−27 51 36.90	4.374	>28.9	25.86 ± 0.08	25.01 ± 0.07	24.87 ± 0.07	...	...	24.73 ± 0.12	25.26 ± 0.27	25.24 ± 0.30	24.22 ± 0.05	24.98 ± 0.16	>22.39	>22.54
S27744	3 32 54.04	−27 50 00.79	4.430	>28.9	25.93 ± 0.06	24.95 ± 0.06	25.06 ± 0.06	...	...	25.33 ± 0.09	25.29 ± 0.13	24.98 ± 0.09	24.80 ± 0.12	25.20 ± 0.25	>22.39	>22.54

Table 1
(Continued)

ID	R.A.	Decl.	$z_{\rm spec}$	B	V	i	z	F110W	F160W	J	H	K	3.6 μm	4.5 μm	5.8 μm	8.0 μm
S28132	3 32 55.25	−27 50 22.46	4.169	29.14 ± 1.50	25.27 ± 0.06	24.49 ± 0.06	24.42 ± 0.06	...	...	24.29 ± 0.04	24.19 ± 0.05	23.86 ± 0.04	23.55 ± 0.06	23.83 ± 0.09	23.74 ± 0.43	23.29 ± 0.32
S28613	3 32 57.17	−27 51 45.01	4.760	28.32 ± 0.71	26.02 ± 0.09	24.60 ± 0.06	24.64 ± 0.06	...	...	24.98 ± 0.07	24.78 ± 0.07	24.45 ± 0.07	24.13 ± 0.06	24.54 ± 0.14	>22.39	26.70 ± 8.13
N1404	12 35 57.43	62 14 08.82	4.196	>28.9	25.43 ± 0.08	24.45 ± 0.07	24.20 ± 0.06	...	...	23.98 ± 0.15	...	23.22 ± 0.17	22.72 ± 0.06	22.96 ± 0.10	22.56 ± 0.15	23.14 ± 0.27
N1922	12 36 01.25	62 13 19.21	3.887	28.00 ± 0.39	26.07 ± 0.07	25.52 ± 0.08	25.43 ± 0.08	...	...	25.96 ± 0.48	...	24.96 ± 0.42	25.39 ± 0.17	25.79 ± 0.38	>22.39	>22.54
N3415	12 36 09.70	62 11 11.00	3.946	27.64 ± 0.41	25.03 ± 0.06	24.59 ± 0.06	24.58 ± 0.06	...	...	25.52 ± 0.57	...	>24.27	23.89 ± 0.07	24.04 ± 0.09	24.68 ± 0.92	>22.54
N5886	12 36 20.27	62 12 11.51	4.061	29.14 ± 1.00	26.03 ± 0.08	25.48 ± 0.07	25.51 ± 0.08	...	...	24.03 ± 0.19	...	>24.27	24.46 ± 0.09	24.67 ± 0.14	>22.39	>22.54
N6333	12 36 21.94	62 15 17.12	4.890	>28.9	26.67 ± 0.15	25.11 ± 0.08	24.92 ± 0.07	...	...	24.82 ± 0.28	...	24.12 ± 0.25	23.45 ± 0.06	23.70 ± 0.07	24.18 ± 0.82	>22.54
N6660	12 36 23.23	62 12 35.80	4.338	28.09 ± 0.38	25.93 ± 0.07	25.51 ± 0.07	25.42 ± 0.07	...	...	>24.57	...	>24.27	24.45 ± 0.08	25.22 ± 0.22	>22.39	>22.54
N6738	12 36 23.56	62 15 20.30	4.889	>28.9	28.15 ± 0.25	26.19 ± 0.08	26.09 ± 0.08	...	...	>24.57	...	>24.27	24.44 ± 0.08	25.07 ± 0.18	>22.39	>22.54
N7372	12 36 25.92	62 09 03.95	4.146	>28.9	24.50 ± 0.05	23.58 ± 0.05	23.51 ± 0.05	...	...	23.48 ± 0.07	...	23.33 ± 0.12	23.00 ± 0.06	23.40 ± 0.07	>22.39	>22.54
N10307	12 36 36.44	62 16 20.31	4.049	>28.9	26.12 ± 0.06	25.73 ± 0.06	25.71 ± 0.07	...	...	>24.57	...	>24.27	23.66 ± 0.06	23.90 ± 0.07	>22.39	23.26 ± 0.20
N10416	12 36 36.82	62 12 04.30	4.000	27.34 ± 0.33	25.74 ± 0.08	25.05 ± 0.07	24.94 ± 0.07	...	...	24.35 ± 0.31	...	22.93 ± 0.17	22.76 ± 0.06	22.95 ± 0.06	22.87 ± 0.16	23.49 ± 0.32
N12074	12 36 42.05	62 13 31.74	4.424	27.03 ± 0.25	26.43 ± 0.15	25.54 ± 0.11	25.18 ± 0.09	24.60 ± 0.03	23.41 ± 0.01	23.62 ± 0.10	...	22.41 ± 0.07	21.78 ± 0.05	21.57 ± 0.05	21.21 ± 0.06	21.27 ± 0.06
N12138	12 36 42.25	62 15 23.25	4.414	29.14 ± 2.62	26.42 ± 0.18	24.66 ± 0.08	24.47 ± 0.07	...	...	24.40 ± 0.17	...	23.51 ± 0.15	23.09 ± 0.06	23.36 ± 0.06	23.30 ± 0.19	23.32 ± 0.21
N12849	12 36 44.68	62 11 50.62	4.580	28.53 ± 1.14	26.82 ± 0.26	25.27 ± 0.10	24.96 ± 0.08	24.97 ± 0.03	24.69 ± 0.03	25.51 ± 0.52	...	24.27 ± 0.24	23.00 ± 0.06	23.23 ± 0.06	22.84 ± 0.16	>22.54
N13279	12 36 46.16	62 07 01.83	4.444	28.80 ± 1.09	26.07 ± 0.09	24.89 ± 0.06	24.88 ± 0.07	...	...	25.05 ± 0.16	...	24.48 ± 0.22	23.96 ± 0.07	24.25 ± 0.13	>22.39	>22.54
N13347	12 36 46.38	62 15 13.75	4.063	28.32 ± 0.35	26.17 ± 0.07	25.69 ± 0.07	25.78 ± 0.07	...	25.38 ± 0.19	>24.57	...	>24.27	24.84 ± 0.08	25.75 ± 0.39	>22.39	>22.54
N13950	12 36 48.41	62 16 43.29	4.076	28.70 ± 1.50	25.22 ± 0.07	24.42 ± 0.06	24.33 ± 0.06	...	...	24.95 ± 0.41	...	23.77 ± 0.24	23.42 ± 0.06	23.67 ± 0.07	23.85 ± 0.31	23.62 ± 0.27
N15819	12 36 54.04	62 08 55.46	3.985	27.74 ± 0.52	25.33 ± 0.07	24.27 ± 0.06	24.19 ± 0.06	...	...	24.32 ± 0.12	...	23.70 ± 0.15	23.07 ± 0.06	23.50 ± 0.07	23.14 ± 0.22	23.11 ± 0.25
N16443	12 36 55.94	62 14 12.76	4.085	26.85 ± 0.24	24.74 ± 0.06	23.95 ± 0.06	23.78 ± 0.05	24.05 ± 0.02	23.57 ± 0.01	23.64 ± 0.13	...	22.76 ± 0.12	22.54 ± 0.06	22.59 ± 0.06	22.52 ± 0.10	22.38 ± 0.10
N17998	12 37 00.66	62 17 56.36	3.852	29.45 ± 1.83	26.29 ± 0.11	25.23 ± 0.08	25.10 ± 0.07	...	...	24.78 ± 0.27	...	23.73 ± 0.19	23.64 ± 0.06	23.84 ± 0.08	23.90 ± 0.42	>22.54
N19290	12 37 05.01	62 17 31.34	3.924	28.62 ± 0.77	25.39 ± 0.06	24.74 ± 0.06	24.62 ± 0.06	...	...	24.20 ± 0.15	...	23.57 ± 0.18	22.97 ± 0.06	23.26 ± 0.07	23.23 ± 0.23	>22.54
N20633	12 37 09.77	62 14 00.67	3.910	26.05 ± 0.12	25.44 ± 0.07	25.27 ± 0.09	25.20 ± 0.09	...	...	25.50 ± 0.50	...	24.60 ± 0.50	23.86 ± 0.06	24.05 ± 0.08	>22.39	>22.54
N21086	12 37 11.48	62 21 55.83	4.058	28.90 ± 1.70	25.04 ± 0.07	23.99 ± 0.06	23.66 ± 0.05	...	...	23.61 ± 0.09	...	22.92 ± 0.10	22.34 ± 0.06	22.73 ± 0.06	22.64 ± 0.17	22.33 ± 0.13
N21565	12 37 13.04	62 21 11.49	4.047	28.09 ± 0.90	25.35 ± 0.09	24.32 ± 0.06	24.09 ± 0.06	...	23.74 ± 0.10	24.39 ± 0.16	...	23.27 ± 0.12	22.55 ± 0.06	22.68 ± 0.06	22.76 ± 0.17	22.47 ± 0.14
N23039	12 37 18.07	62 16 41.72	4.822	>28.9	27.42 ± 0.18	25.74 ± 0.08	25.77 ± 0.08	...	...	25.84 ± 0.39	...	>24.27	24.36 ± 0.08	25.04 ± 0.19	>22.39	>22.54
N23308	12 37 18.97	62 10 26.21	4.134	>28.9	27.54 ± 0.14	26.31 ± 0.08	26.68 ± 0.10	...	...	25.73 ± 0.64	...	23.79 ± 0.23	22.76 ± 0.06	23.00 ± 0.06	22.59 ± 0.13	22.34 ± 0.11
N23314	12 37 19.00	62 19 53.84	4.190	29.89 ± 2.75	25.12 ± 0.06	24.45 ± 0.06	24.38 ± 0.06	...	...	24.51 ± 0.13	...	24.13 ± 0.20	24.19 ± 0.08	24.56 ± 0.14	24.22 ± 0.60	>22.54
N23791	12 37 20.58	62 11 06.11	4.421	>28.9	25.44 ± 0.07	24.23 ± 0.06	24.16 ± 0.05	...	...	23.82 ± 0.16	...	23.18 ± 0.19	23.26 ± 0.06	23.68 ± 0.07	23.58 ± 0.26	23.54 ± 0.27
N23868	12 37 20.84	62 18 43.52	4.072	28.15 ± 0.50	26.26 ± 0.10	25.48 ± 0.08	25.42 ± 0.08	...	...	>24.57	...	>24.27	23.21 ± 0.06	23.34 ± 0.07	23.32 ± 0.26	>22.54
N24628	12 37 23.57	62 20 38.72	4.502	30.21 ± 2.67	26.58 ± 0.11	25.46 ± 0.07	25.28 ± 0.07	...	...	24.49 ± 0.39	...	>24.27	23.57 ± 0.06	24.08 ± 0.10	23.75 ± 0.39	>22.54
N25752	12 37 28.03	62 19 54.01	4.152	28.09 ± 0.71	26.08 ± 0.11	24.98 ± 0.08	24.80 ± 0.08	...	...	25.26 ± 0.22	...	24.15 ± 0.19	23.42 ± 0.06	23.56 ± 0.08	23.31 ± 0.26	23.01 ± 0.22
N31130	12 37 57.51	62 17 19.10	4.680	>28.9	25.70 ± 0.10	24.00 ± 0.06	23.82 ± 0.06	...	...	23.85 ± 0.09	...	23.65 ± 0.18	22.94 ± 0.06	23.33 ± 0.07	23.36 ± 0.29	23.07 ± 0.23

Notes. The observed flux is given in units of AB magnitude and magnitude error for each filter. The B-, V-, i-, and z-band magnitudes indicate the *HST*/ACS F435W, F606W, F775W, and F850LP magnitudes. The $F110W$- and $F160W$-band magnitudes are from *HST*/NICMOS. The J-, H-, and K-band magnitudes are the VLT/ISAAC magnitudes for galaxies in CDF-South, while J- and K-band magnitudes are from CFHT/WIRCAM for galaxies in HDF-North. Two of the objects, S15920 and N12074, appear to show multiwavelength SED that are inconsistent with their quoted redshift and likely have erroneous spectroscopic redshifts.

Table 2
Spectral Energy Distribution-fitting Results

ID	$z_{\rm spec}$	χ^2	$\log_{10} M_*$ ($M_\odot$)	$E(B-V)$	Age (Myr)	τ (Myr)	β	Extinction Law	$\log_{10} L_{\rm H\alpha}$ (erg s^{-1})	EW$_{\rm H\alpha}$ (Å)	SFR$_{\rm H\alpha}$ ($M_\odot$ yr^{-1})	SFR$_{\rm UV}$ ($M_\odot$ yr^{-1})	$S_{\rm ch1}$
S1213	4.017	0.48	9.66	0.37	6	100	−1.25	SB	43.25 ± 0.15	362 ± 93	141.9	10.6	11.80
...	...	0.66	9.76	0.17	91	800	−0.98	SMC	42.98 ± 0.35	449 ± 100	76.1	10.7	12.69
S1461	3.912	2.02	9.85	0.18	69	1000	−1.80	SB	43.46 ± 0.02	896 ± 72	228.6	20.1	13.76
...	...	1.89	9.84	0.07	170	900	−1.79	SMC	43.38 ± 0.02	1285 ± 106	188.7	20.6	16.74
S1478	4.825	3.08	10.99	0.04	701	400	−1.97	SB	43.84 ± 0.07	743 ± 69	548.8	54.2	10.16
...	...	3.20	11.01	0.01	822	400	−1.98	SMC	43.78 ± 0.08	705 ± 68	474.0	54.3	9.29
S1944	3.939	0.89	10.05	0.34	14	200	−1.29	SB	43.66 ± 0.03	423 ± 62	361.9	24.1	9.44
...	...	0.62	10.25	0.09	243	300	−1.51	SMC	43.56 ± 0.04	1006 ± 112	284.8	24.4	20.17
S4142	4.912	0.80	9.62	0.09	99	100	−2.09	SB	42.89 ± 0.25	594 ± 269	61.4	14.7	11.49
...	...	3.00	8.86	0.11	3	1000	−1.99	SMC	43.15 ± 0.12	2557 ± 825	111.1	16.3	12.70
S4168	3.828	0.90	9.79	0.30	39	700	−1.34	SB	43.69 ± 0.08	1314 ± 203	382.8	9.1	12.98
...	...	2.82	9.82	0.17	121	900	−0.89	SMC	43.47 ± 0.14	1341 ± 201	231.1	9.0	7.06
S4773	4.292	0.26	9.62	0.37	5	100	−1.27	SB	43.22 ± 0.10	367 ± 64	129.6	9.8	24.26
...	...	0.64	9.66	0.17	70	800	−0.97	SMC	42.91 ± 0.24	406 ± 66	64.2	10.2	18.06
S5533	4.738	3.09	8.83	0.15	4	800	−2.32	SB	42.62 ± 0.14	584 ± 204	32.8	13.8	5.16
...	...	4.43	8.63	0.06	1	900	−2.58	SMC	42.81 ± 0.09	3644 ± 1100	50.6	14.2	10.61
S6665	3.891	3.46	9.32	0.17	23	900	−1.99	SB	42.40 ± 0.65	156 ± 118	19.6	16.4	0.64
...	...	5.76	8.93	0.13	4	1000	−1.77	SMC	42.88 ± 0.19	876 ± 150	60.2	17.0	5.92
S6854	4.600	0.70	9.52	0.29	9	500	−1.55	SB	43.34 ± 0.04	587 ± 102	174.7	14.1	17.17
...	...	0.61	9.65	0.14	69	800	−1.28	SMC	43.12 ± 0.07	660 ± 106	103.5	14.6	19.87
S6867	4.414	0.69	9.81	0.31	19	300	−1.35	SB	43.59 ± 0.04	737 ± 82	307.9	14.0	24.39
...	...	0.69	9.81	0.17	71	1000	−1.00	SMC	43.35 ± 0.07	792 ± 80	175.0	14.8	25.40
S8067	4.431	0.64	9.69	0.25	8	200	−1.74	SB	43.32 ± 0.07	382 ± 54	166.9	32.1	15.14
...	...	0.82	9.92	0.09	101	1000	−1.66	SMC	43.12 ± 0.12	444 ± 71	104.7	32.2	15.21
S8787	4.254	23.00	10.08	0.36	5	60	−1.35	SB	43.73 ± 0.04	416 ± 66	421.1	33.6	2.43
...	...	2.65	9.76	0.22	8	500	−0.78	SMC	43.54 ± 0.07	543 ± 79	273.7	35.2	9.23
S9738	4.788	2.34	9.92	0.10	95	10	−1.60	SB	43.07 ± 0.10	731 ± 155	93.6	7.3	10.53
...	...	1.67	9.17	0.22	9	700	−0.68	SMC	43.17 ± 0.08	825 ± 178	117.8	7.8	14.42
S10232	4.900	0.25	9.51	0.30	8	50	−1.50	SB	43.26 ± 0.13	499 ± 137	144.8	12.8	12.46
...	...	0.38	9.67	0.14	80	700	−1.27	SMC	42.99 ± 0.30	516 ± 120	77.2	13.5	9.88
S10340	4.440	1.15	9.60	0.31	6	300	−1.51	SB	43.38 ± 0.06	538 ± 68	189.1	16.5	14.62
...	...	0.55	9.64	0.14	56	900	−1.32	SMC	43.14 ± 0.11	642 ± 78	108.8	17.3	24.23
S10388	4.500	0.54	10.03	0.46	5	200	−0.91	SB	43.87 ± 0.01	650 ± 74	580.3	11.6	27.37
...	...	0.27	10.04	0.23	75	700	−0.40	SMC	43.47 ± 0.02	647 ± 74	232.9	11.9	35.23
S12424	4.068	2.03	10.18	0.25	54	400	−1.51	SB	43.21 ± 0.17	214 ± 54	128.1	25.7	3.23
...	...	2.11	10.28	0.06	364	400	−1.82	SMC	43.26 ± 0.15	590 ± 88	143.6	26.1	7.45
S12652	4.384	5.52	9.90	0.18	80	1000	−1.79	SB	42.66 ± 0.43	139 ± 67	36.1	19.8	0.95
...	...	3.20	10.12	0.00	541	400	−2.64	SMC	42.66 ± 0.43	338 ± 182	36.3	17.7	3.16
S13025	4.333	7.02	11.51	0.00	845	1	0.76	SB	43.87 ± 0.09	583 ± 60	590.9	4.4	26.40
...	...	7.70	11.43	0.42	71	1	2.00	SMC	44.10 ± 0.05	226 ± 40	985.2	5.7	10.53
S13297	4.271	2.36	10.32	0.19	335	800	−1.57	SB	43.43 ± 0.04	698 ± 62	211.9	11.8	22.84
...	...	3.69	10.31	0.10	571	1000	−1.35	SMC	43.26 ± 0.06	667 ± 62	143.5	12.2	17.07
S13701	4.000	1.38	9.60	0.30	19	600	−1.40	SB	42.99 ± 0.10	289 ± 83	77.4	9.9	5.63
...	...	0.15	9.71	0.15	95	700	−1.09	SMC	42.79 ± 0.17	332 ± 84	48.3	10.4	20.90
S14097	4.597	0.45	9.57	0.26	22	600	−1.56	SB	42.74 ± 0.40	192 ± 90	43.5	11.9	4.02
...	...	1.90	9.19	0.18	9	800	−1.10	SMC	42.65 ± 0.61	256 ± 99	34.9	13.2	3.45
S14602[a,b]	4.762	9.93	10.77	0.41	50	60	−0.77	SB	43.56 ± 0.16	128 ± 28	285.7	19.5	0.68
...	...	22.50	10.68	0.28	83	90	0.13	SMC	...	...	...	21.8	−2.10
S15920	4.005	72.89	11.03	0.00	699	60	−0.36	SB	42.74 ± 0.55	107 ± 25	43.5	5.9	0.32
...	...	10.09	10.41	0.56	5	30	2.43	SMC	...	...	...	3.8	−2.75
S17126	4.063	1.91	10.44	0.39	80	600	−0.87	SB	43.60 ± 0.08	349 ± 45	313.4	9.5	6.90
...	...	3.35	10.32	0.31	76	300	0.42	SMC	42.91 ± 0.67	95 ± 30	63.9	8.2	0.17
S17403	4.900	0.84	9.90	0.44	8	90	−0.91	SB	43.51 ± 0.05	354 ± 95	254.2	8.9	19.44
...	...	0.72	10.19	0.14	363	800	−1.02	SMC	43.17 ± 0.11	548 ± 104	117.8	9.5	27.08
S17579	4.724	8.58	11.14	0.26	115	1	−0.77	SB	43.52 ± 0.02	147 ± 3	263.2	17.3	5.12
...	...	8.60	10.98	0.10	378	80	−0.88	SMC	43.55 ± 0.02	305 ± 40	281.9	18.3	16.02
S17728	4.640	1.19	9.98	0.27	99	600	−1.36	SB	43.12 ± 0.10	384 ± 76	104.3	8.1	9.20
...	...	1.06	9.97	0.09	414	800	−1.48	SMC	42.98 ± 0.14	645 ± 86	75.8	9.5	13.47
S17994	4.142	0.70	10.10	0.26	34	400	−1.52	SB	43.58 ± 0.05	465 ± 55	297.7	29.6	16.51
...	...	0.46	10.20	0.09	207	600	−1.59	SMC	43.45 ± 0.07	760 ± 93	223.7	30.5	26.52
S20830	4.000	1.71	10.06	0.26	77	500	−1.43	SB	43.40 ± 0.08	526 ± 86	197.7	13.5	10.63
...	...	0.26	9.95	0.19	80	900	−0.73	SMC	43.13 ± 0.15	371 ± 80	107.4	13.8	19.51
S21686	4.773	0.83	9.49	0.29	9	300	−1.53	SB	43.34 ± 0.06	635 ± 118	173.4	12.4	16.11

Table 2
(Continued)

ID	$z_{\rm spec}$	χ^2	$\log_{10} M_*$ ($M_\odot$)	$E(B-V)$	Age (Myr)	τ (Myr)	β	Extinction Law	$\log_{10} L_{\rm H\alpha}$ (erg s^{-1})	EW$_{\rm H\alpha}$ (Å)	SFR$_{\rm H\alpha}$ ($M_\odot$ yr^{-1})	SFR$_{\rm UV}$ ($M_\odot$ yr^{-1})	$S_{\rm ch1}$
...	...	1.40	9.63	0.13	80	800	−1.33	SMC	43.11 ± 0.12	754 ± 118	102.3	13.2	13.65
S21819	4.120	0.50	9.40	0.09	99	500	−2.19	SB	43.12 ± 0.04	1459 ± 181	103.8	12.4	31.55
...	...	4.87	8.76	0.09	1	900	−2.29	SMC	43.29 ± 0.03	8470 ± 855	155.5	13.2	17.02
S22255	4.058	0.27	9.27	0.26	8	500	−1.72	SB	42.94 ± 0.18	420 ± 144	68.6	11.6	15.55
...	...	4.45	8.98	0.17	5	800	−1.37	SMC	43.00 ± 0.15	1011 ± 201	79.8	12.1	8.62
S22746	4.049	6.16	10.29	0.08	739	700	−1.92	SB	43.26 ± 0.10	880 ± 144	142.6	10.8	7.12
...	...	5.79	10.12	0.09	469	900	−1.51	SMC	43.24 ± 0.10	885 ± 146	137.9	11.3	7.59
S23040	4.400	1.50	9.72	0.25	65	500	−1.52	SB	43.35 ± 0.04	932 ± 193	175.2	8.2	15.11
...	...	0.56	9.57	0.17	70	700	−1.01	SMC	43.16 ± 0.07	897 ± 178	114.8	8.7	23.97
S23745	4.923	0.89	9.93	0.19	71	800	−1.78	SB	43.22 ± 0.10	440 ± 81	130.2	22.2	11.77
...	...	0.10	10.20	0.01	637	900	−2.19	SMC	43.03 ± 0.16	555 ± 89	84.8	22.2	36.11
S23763[a]	4.931	24.24	10.80	0.28	91	90	−1.29	SB	43.74 ± 0.05	261 ± 19	433.6	42.9	6.17
...	...	24.87	10.72	0.06	189	50	−1.50	SMC	43.60 ± 0.07	478 ± 47	311.9	44.9	8.84
S24739	4.020	0.68	9.43	0.23	14	700	−1.74	SB	43.07 ± 0.07	453 ± 73	93.0	15.3	13.64
...	...	5.71	9.11	0.17	5	800	−1.36	SMC	43.16 ± 0.06	1060 ± 180	113.0	16.1	9.52
S25586	4.374	1.17	9.11	0.18	6	1000	−2.09	SB	43.12 ± 0.05	920 ± 152	103.3	17.9	23.97
...	...	1.70	8.90	0.11	4	600	−1.92	SMC	43.06 ± 0.05	1393 ± 398	90.9	19.2	24.85
S27744	4.430	0.35	9.09	0.08	30	900	−2.32	SB	42.61 ± 0.19	493 ± 193	32.0	17.1	10.49
...	...	2.36	8.80	0.07	1	800	−2.47	SMC	42.94 ± 0.08	3408 ± 566	68.5	17.9	11.36
S28132	4.169	0.59	9.57	0.24	9	700	−1.76	SB	43.18 ± 0.08	357 ± 70	119.9	25.3	11.81
...	...	0.40	9.81	0.08	117	1000	−1.77	SMC	43.05 ± 0.11	518 ± 91	88.6	25.7	19.48
S28613	4.760	2.96	9.21	0.16	6	900	−2.19	SB	43.11 ± 0.08	703 ± 154	101.0	28.9	11.99
...	...	4.71	8.88	0.07	5	900	−2.34	SMC	43.14 ± 0.07	1745 ± 303	108.6	30.0	15.68
N1404	4.196	1.13	10.07	0.36	8	70	−1.26	SB	43.63 ± 0.13	322 ± 69	333.4	27.9	8.03
...	...	1.64	10.21	0.16	107	500	−1.02	SMC	43.44 ± 0.22	498 ± 88	219.1	27.6	10.54
N1922	3.887	0.97	9.12	0.26	3	500	−1.95	SB	42.38 ± 0.78	290 ± 250	19.0	8.5	2.05
...	...	1.45	8.71	0.12	1	900	−2.01	SMC	42.70 ± 0.57	2346 ± 390	39.7	8.7	9.08
N3415	3.946	1.37	9.68	0.12	82	700	−2.06	SB	42.93 ± 0.14	451 ± 90	67.6	20.5	6.98
...	...	1.22	9.66	0.04	175	800	−2.16	SMC	42.96 ± 0.13	743 ± 113	71.6	20.7	10.17
N5886	4.061	3.03	9.19	0.25	9	700	−1.74	SB	42.85 ± 0.17	417 ± 113	56.5	9.8	3.27
...	...	3.98	9.46	0.10	105	800	−1.58	SMC	42.63 ± 0.34	423 ± 105	33.7	9.8	2.85
N6333	4.890	1.86	9.77	0.29	10	90	−1.52	SB	43.48 ± 0.03	465 ± 60	238.9	23.5	8.66
...	...	1.32	10.21	0.04	513	1000	−1.99	SMC	43.26 ± 0.05	793 ± 93	145.0	22.9	14.53
N6660	4.338	5.34	8.76	0.12	10	1000	−2.30	SB	43.08 ± 0.03	1901 ± 545	94.1	11.9	7.87
...	...	9.02	8.68	0.08	1	1000	−2.38	SMC	43.13 ± 0.02	1901 ± 522	105.8	12.2	8.47
N6738	4.889	0.32	9.19	0.27	9	800	−1.65	SB	43.26 ± 0.06	1066 ± 230	144.2	8.1	21.52
...	...	2.94	8.98	0.19	5	600	−1.15	SMC	43.11 ± 0.09	1301 ± 255	101.2	9.2	7.54
N7372	4.146	0.93	10.16	0.32	3	30	−1.73	SB	43.60 ± 0.04	488 ± 48	316.7	55.2	11.68
...	...	0.85	9.76	0.10	34	1000	−1.77	SMC	43.32 ± 0.08	573 ± 59	164.7	55.0	14.06
N10307	4.049	2.01	9.94	0.08	394	300	−1.94	SB	43.27 ± 0.03	1477 ± 125	147.4	8.0	12.99
...	...	1.65	10.14	0.00	1048	600	−2.15	SMC	43.14 ± 0.04	1329 ± 118	109.2	7.8	12.75
N10416	4.000	2.82	10.39	0.09	120	1	−1.51	SB	43.50 ± 0.05	819 ± 101	248.7	14.6	11.16
...	...	2.80	10.36	0.08	602	600	−1.52	SMC	43.57 ± 0.04	1333 ± 138	291.9	14.2	14.71
N12074[a]	4.424	21.30	11.03	0.66	5	10	0.06	SB	...	...	...	16.1	−2.37
...	...	10.50	11.01	0.36	178	300	1.01	SMC	43.88 ± 0.15	304 ± 14	601.2	9.6	2.69
N12138	4.414	1.35	9.98	0.37	5	80	−1.30	SB	43.57 ± 0.02	367 ± 28	292.6	23.7	9.43
...	...	0.89	10.09	0.15	101	700	−1.10	SMC	43.27 ± 0.05	428 ± 35	147.1	24.1	13.55
N12849	4.580	1.14	10.40	0.23	126	80	−1.41	SB	43.67 ± 0.04	760 ± 146	368.3	15.4	20.47
...	...	1.08	10.45	0.08	655	800	−1.50	SMC	43.48 ± 0.07	929 ± 150	240.0	16.0	22.89
N13279	4.444	0.75	9.76	0.13	99	600	−1.98	SB	42.99 ± 0.12	478 ± 111	78.0	18.6	11.83
...	...	5.34	8.99	0.12	5	600	−1.79	SMC	43.22 ± 0.07	1632 ± 312	130.0	20.2	10.53
N13347	4.063	1.25	8.72	0.17	6	800	−2.13	SB	42.95 ± 0.05	1578 ± 465	70.4	8.1	15.34
...	...	3.18	8.66	0.11	1	1000	−2.09	SMC	42.98 ± 0.04	5122 ± 885	75.9	8.4	14.40
N13950	4.076	1.14	9.62	0.25	9	300	−1.71	SB	43.28 ± 0.08	413 ± 65	149.9	24.9	11.17
...	...	1.34	9.77	0.11	70	1000	−1.53	SMC	43.12 ± 0.13	510 ± 75	104.0	25.6	12.71
N15819	3.985	3.77	9.74	0.29	8	400	−1.55	SB	43.58 ± 0.02	620 ± 50	299.9	23.6	8.51
...	...	2.39	9.85	0.13	71	1000	−1.34	SMC	43.38 ± 0.03	773 ± 63	188.6	24.6	12.95
N16443	4.085	15.89	10.19	0.36	11	60	−1.19	SB	43.54 ± 0.31	214 ± 84	276.8	29.3	1.28
...	...	19.65	10.41	0.13	226	500	−1.24	SMC	43.50 ± 0.35	554 ± 180	251.3	30.2	2.96
N17998	3.852	1.59	9.72	0.40	5	30	−1.14	SB	43.39 ± 0.09	438 ± 150	194.2	9.4	5.38
...	...	0.26	9.73	0.19	70	800	−0.76	SMC	43.13 ± 0.17	564 ± 181	106.5	9.5	18.45
N19290	3.924	0.29	9.85	0.33	13	200	−1.34	SB	43.71 ± 0.07	735 ± 119	408.6	17.7	28.83
...	...	2.32	10.03	0.16	105	800	−0.98	SMC	43.45 ± 0.13	743 ± 108	221.6	18.0	10.53

Table 2
(Continued)

ID	$z_{\rm spec}$	χ^2	$\log_{10} M_*$ ($M_\odot$)	$E(B-V)$	Age (Myr)	τ (Myr)	β	Extinction Law	$\log_{10} L_{\rm H\alpha}$ (erg s^{-1})	EW$_{\rm H\alpha}$ (Å)	SFR$_{\rm H\alpha}$ ($M_\odot$ yr^{-1})	SFR$_{\rm UV}$ ($M_\odot$ yr^{-1})	$S_{\rm ch1}$
N20633	3.910	10.46	9.42	0.28	9	500	−1.59	SB	43.23 ± 0.09	579 ± 111	134.6	12.2	3.43
...	...	13.61	9.54	0.12	79	800	−1.44	SMC	43.10 ± 0.13	891 ± 130	99.6	12.4	4.43
N21086	4.058	4.85	10.12	0.34	8	400	−1.33	SB	43.90 ± 0.02	539 ± 44	630.6	36.3	7.17
...	...	2.02	10.28	0.14	114	700	−1.17	SMC	43.68 ± 0.04	750 ± 52	378.7	37.3	14.39
N21565	4.047	2.52	10.13	0.35	13	80	−1.21	SB	43.78 ± 0.01	451 ± 38	472.3	25.1	8.22
...	...	1.96	10.34	0.11	261	600	−1.37	SMC	43.61 ± 0.02	916 ± 56	324.6	26.4	14.72
N23039	4.822	0.94	9.10	0.22	9	800	−1.87	SB	43.24 ± 0.05	1213 ± 248	136.6	10.9	15.94
...	...	3.36	8.64	0.10	4	1000	−1.98	SMC	43.19 ± 0.06	3367 ± 600	121.8	11.4	12.35
N23308[a]	4.134	2.27	10.72	0.29	871	700	−1.03	SB	43.91 ± 0.04	1687 ± 134	641.8	3.6	17.64
...	...	3.97	10.64	0.12	1222	500	−0.81	SMC	43.67 ± 0.08	1644 ± 120	369.7	3.6	12.99
N23314	4.190	0.88	9.34	0.20	4	80	−2.11	SB	42.85 ± 0.26	333 ± 123	56.1	27.0	6.89
...	...	2.18	9.02	0.10	5	1000	−2.01	SMC	42.94 ± 0.20	795 ± 180	68.1	28.2	9.73
N23791	4.421	1.17	9.73	0.26	6	600	−1.74	SB	43.41 ± 0.04	440 ± 60	205.4	36.2	11.90
...	...	0.64	9.79	0.10	52	1000	−1.64	SMC	43.23 ± 0.06	544 ± 66	134.6	37.4	19.51
N23868	4.072	1.27	9.86	0.41	9	30	−0.99	SB	43.64 ± 0.02	528 ± 66	343.3	9.5	9.92
...	...	0.58	10.32	0.07	859	800	−1.59	SMC	43.36 ± 0.05	1132 ± 97	179.5	9.6	22.32
N24628	4.502	1.48	9.59	0.30	11	300	−1.46	SB	43.54 ± 0.05	840 ± 100	274.3	13.2	14.27
...	...	1.43	9.83	0.11	179	1000	−1.49	SMC	43.29 ± 0.09	1106 ± 113	155.1	13.5	16.49
N25752	4.152	2.14	9.97	0.27	54	600	−1.46	SB	43.35 ± 0.07	471 ± 62	174.9	14.4	8.39
...	...	2.70	9.98	0.13	181	1000	−1.29	SMC	43.20 ± 0.09	636 ± 74	125.8	15.0	8.58
N31130	4.680	1.59	10.15	0.14	82	1000	−1.97	SB	43.50 ± 0.04	567 ± 68	247.6	49.2	13.41
...	...	1.30	10.09	0.09	101	900	−1.75	SMC	43.35 ± 0.05	498 ± 62	174.9	52.9	13.02

Notes.
[a] X-ray detected active galactic nuclei.
[b] Submillimeter galaxy with $f_{850\,\mu\rm m} \sim 5$ mJy (Coppin et al. 2009).

The photometry of each galaxy used in SED fitting is presented in Table 1, as described in Section 2.2. We also list the output parameters from SED fitting in Table 2: stellar mass, $E(B-V)$, stellar population age, e-folding timescale of star formation τ, and UV spectral slope β. These parameters are derived independently for both SB and SMC extinction laws. We derived the UV-slope β by fitting the best-fit model spectra at UV wavelengths (1500–2500 Å) using a power law ($f_\lambda \propto \lambda^\beta$).

The templates used in the SED fitting (CB07; Bruzual 2007) do not incorporate a contribution from nebular emission. As we mentioned in Section 2.1, most of the strong nebular emission lines [O II], Hβ and [O III] fall in the gap between the filters at this redshift range and thus do not affect the broadband photometry at other wavelengths or have a negligible contribution to the broadband flux density, typically of order <10%. The role of nebular continuum on the other hand, begins to be significant at the 20% level only longward of 4.5 μm in the observed frame for young, star-forming galaxies (Zackrisson et al. 2008). Therefore, we conclude that our SED fits to the photometry with the exception of the IRAC ch1 flux density is a reasonable approach to determine the stellar population properties of $3.8 < z_{\rm spec} < 5.0$ galaxies, with negligibly small effects from nebular continuum emission and line emission other than Hα.

Since a number of studies claim the significance of an old stellar component in high-redshift galaxies, especially for red and massive galaxies (e.g., Muzzin et al. 2009), we tested a two-component stellar population model fits for these galaxies. The two-component model is made up of the sum of a young stellar population and an old stellar population. We used a 5 Myr old stellar population forming stars at a constant rate of 30 $M_\odot$ yr^{-1} as the young component, and a single burst, passively evolving stellar population with $z_f = 20$ as the old component. The SED fitting procedure was the same as the case of single-component SED fitting, except the stellar mass ratio between the two component is a free parameter in the two-component SED fitting. Most of the galaxies prefer the single-component fits while only ∼10% of the galaxies show lower χ^2 values for two-component fitting. The galaxies that prefer the two-component fitting have relatively large χ^2 values compared to other objects, i.e., $\chi^2 > 5$, suggesting biases in the photometry of the sources themselves. Therefore, we only use the results from single-component fitting in the following analysis.

In Figure 2, we present the best-fit SED fitting results for all 74 galaxies at $3.8 < z < 5.0$. The filled squares are the observed photometry points given in Table 1, and the overplotted lines are the best-fit SED templates. The best-fit parameters—dust extinction, stellar population age—are shown along with the χ^2 value. In addition to the comparison between the best-fit SED and the multi-band photometry data points, a "residual plot" showing the differences between the observed flux density and the model flux density, as a function of wavelength, is included for each object. The y-axis in the residual plot indicates $(f_{\rm obs} - f_{\rm mod})/\sigma_{\rm obs}$, i.e., the discrepancy between the model flux density and the observed flux density divided by the observed flux density error.

Clearly, a large fraction of our sample galaxies show a significant excess in *Spitzer*/IRAC ch1 (3.6 μm; Figure 2), while no excess is observed in other filters. To quantify this excess in a particular filter, for instance in *Spitzer*/IRAC ch1, we define a significance factor S as follows:

$$S_{\rm ch1} = \frac{\Delta_{\rm ch1}}{\frac{1}{N}\sqrt{\sum_i^{\rm filter} \Delta_i^2}}. \quad (2)$$

In this equation, Δ is defined as $\Delta = (f_{\rm obs} - f_{\rm mod})/\sigma_{\rm obs}$. The denominator indicates the mean of the residuals in filters other than the IRAC ch1—this is basically an indicator showing the

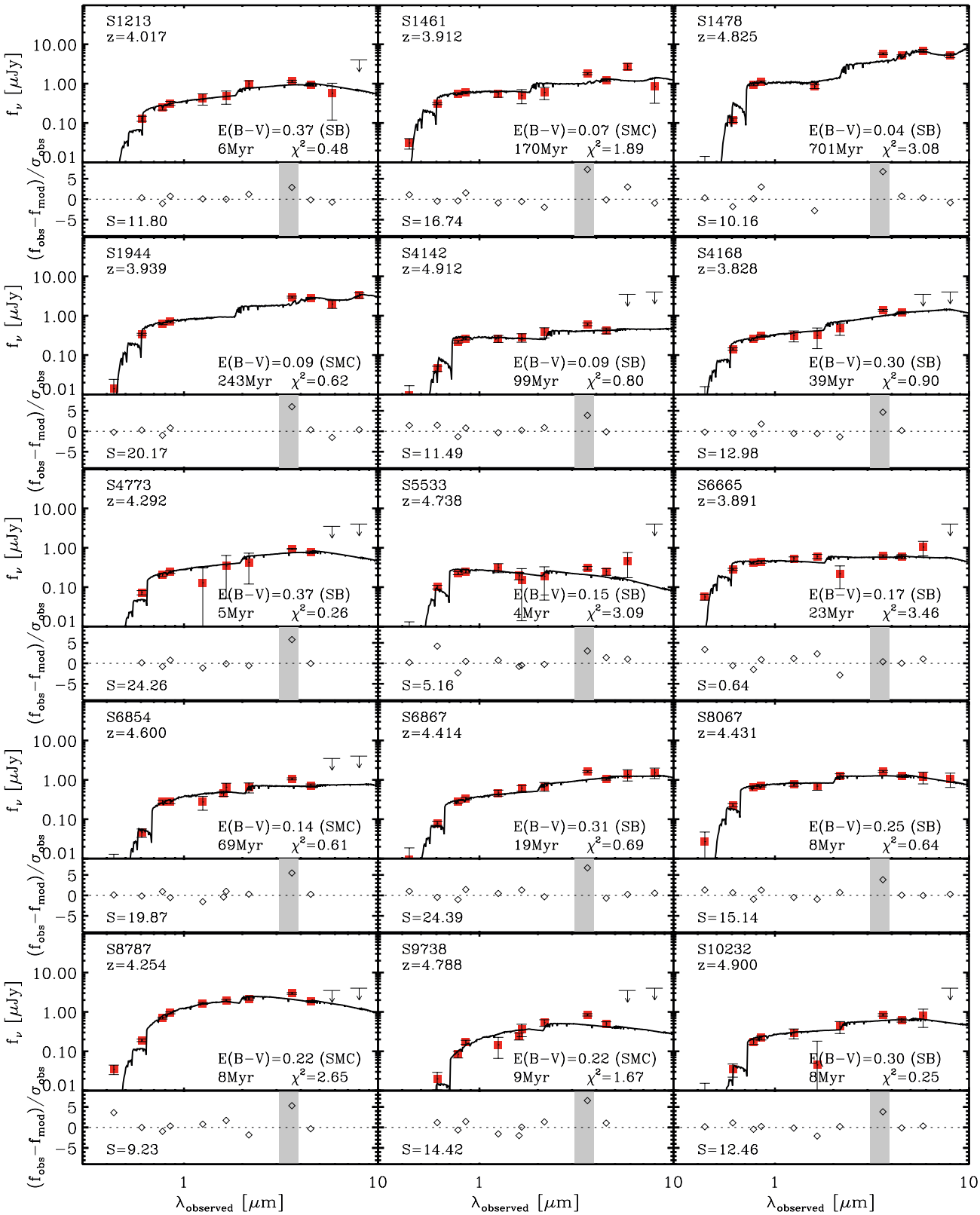

Figure 2. SEDs of galaxies at $3.8 < z_{\rm spec} < 5.0$ over the GOODS fields (first 43 from GOODS-South, next 31 from GOODS-North). The filled squares indicate *HST*/ACS *B*-, *V*-, *i*-, and *z*-band photometry, *J*-, *H*-, and *K*-band photometry for objects selected in GOODS-South, *J*- and *K*-band photometry for objects in GOODS-North, and *Spitzer*/IRAC four-band photometry. For some objects, *HST*/NICMOS F110W/F160W photometry points are available. For objects that are not detected in NIR bands or *Spitzer*/IRAC ch 3/4, we use the 3σ flux density upper limits marked as arrows. Overplotted solid lines are the best-fit galaxy spectral templates (CB07; Bruzual 2007). The best-fit galaxy age, $E(B-V)$, and the extinction law is specified in addition to the lowest χ^2 value. Below each SED, we show the fitting residuals as a function of wavelength. The *y*-axis indicates the residuals divided by the observational flux uncertainty (i.e., $(f_{\rm obs} - f_{\rm mod})/\sigma_{\rm obs}$). The significance factor for the 3.6 μm band flux density excess, *S* (see the text for definition) is also provided. For some objects with $(f_{\rm obs} - f_{\rm mod})/\sigma_{\rm obs}$ at 3.6 μm exceeding the *y*-axis range, we use a triangle in the residual plot and also indicate the value. Two of the objects, S15920 and N12074, appear to show multiwavelength SED that are inconsistent with their quoted redshift and likely have erroneous spectroscopic redshifts.

(A color version of this figure is available in the online journal.)

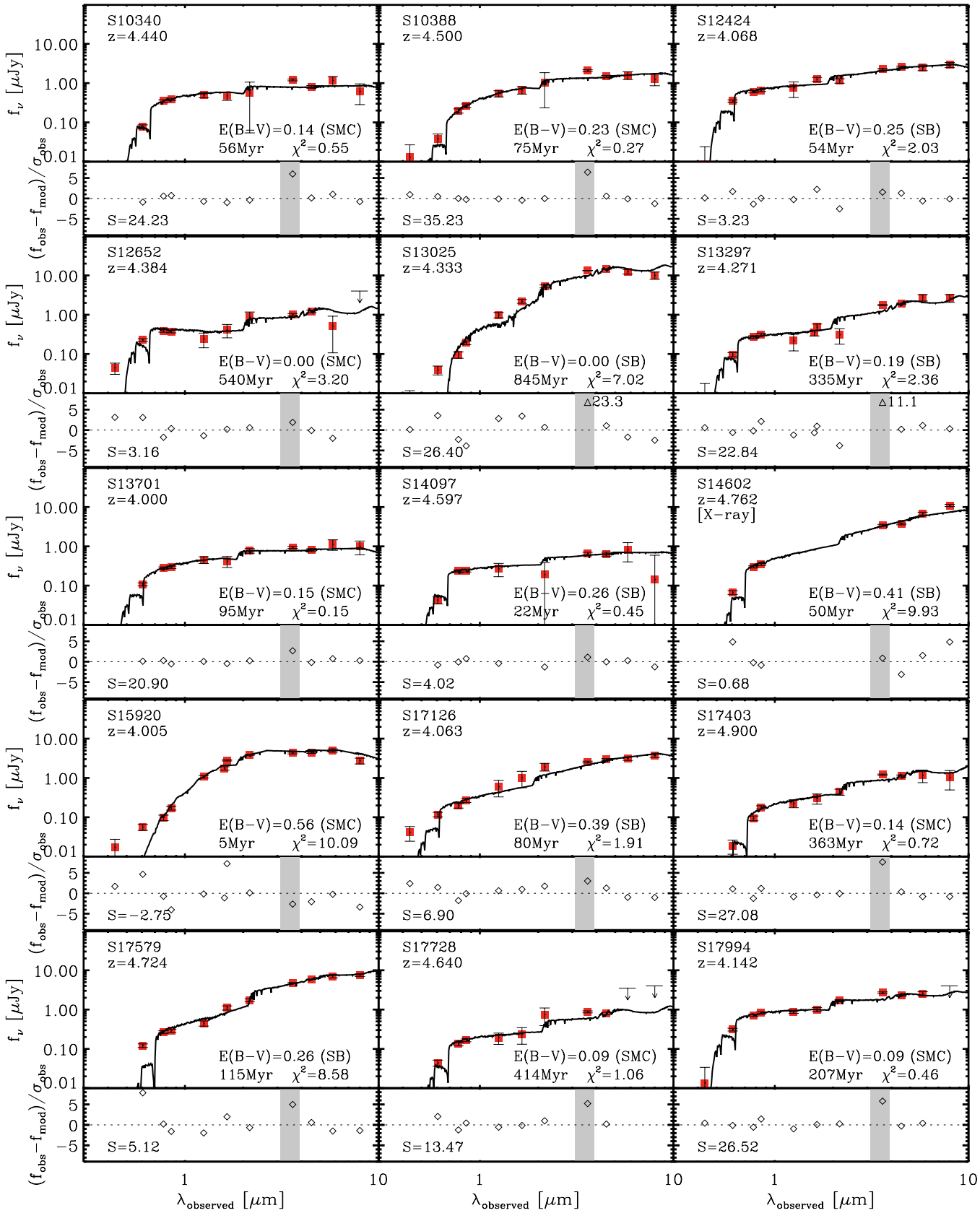

Figure 2. (Continued)

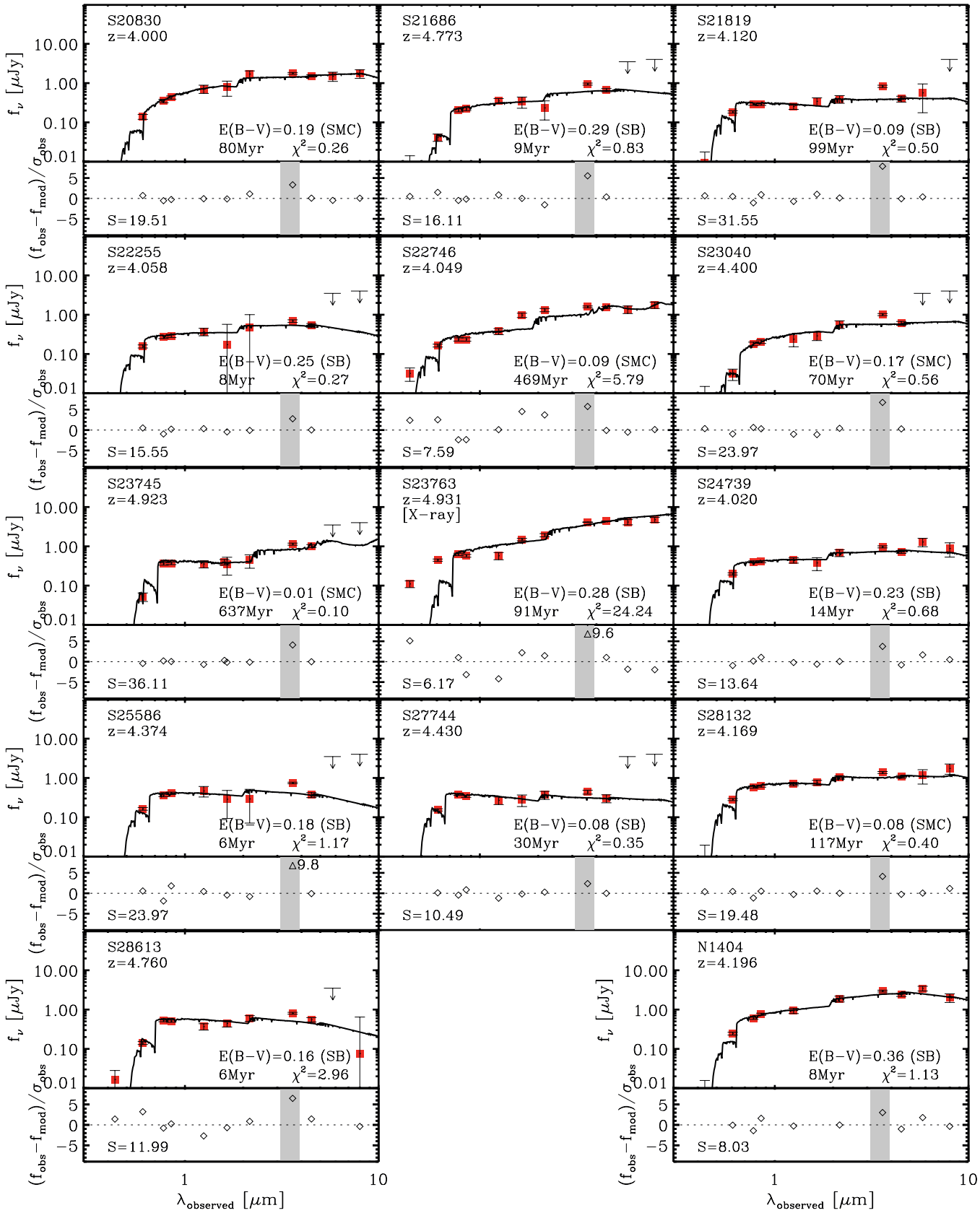

Figure 2. (Continued)

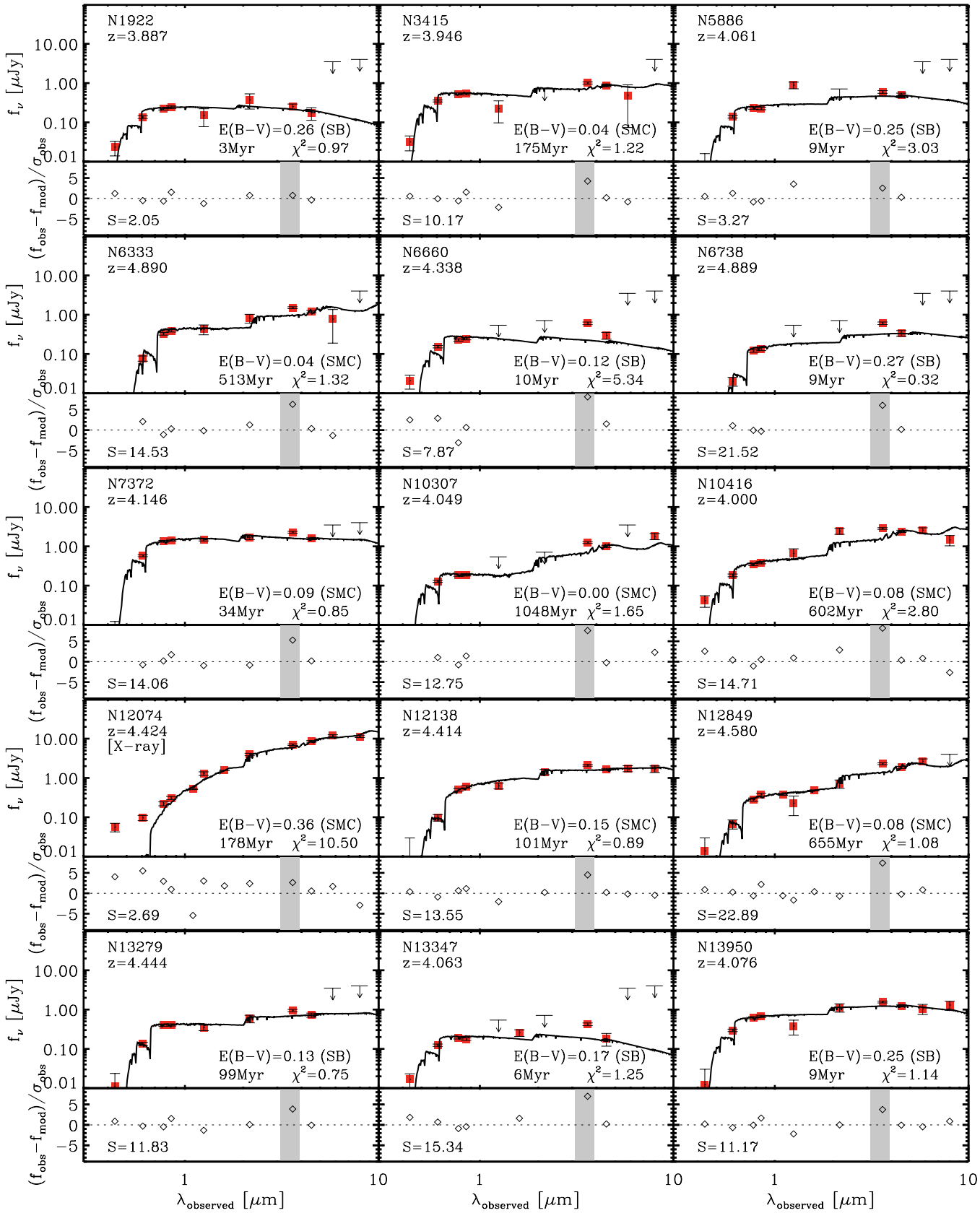

Figure 2. (Continued)

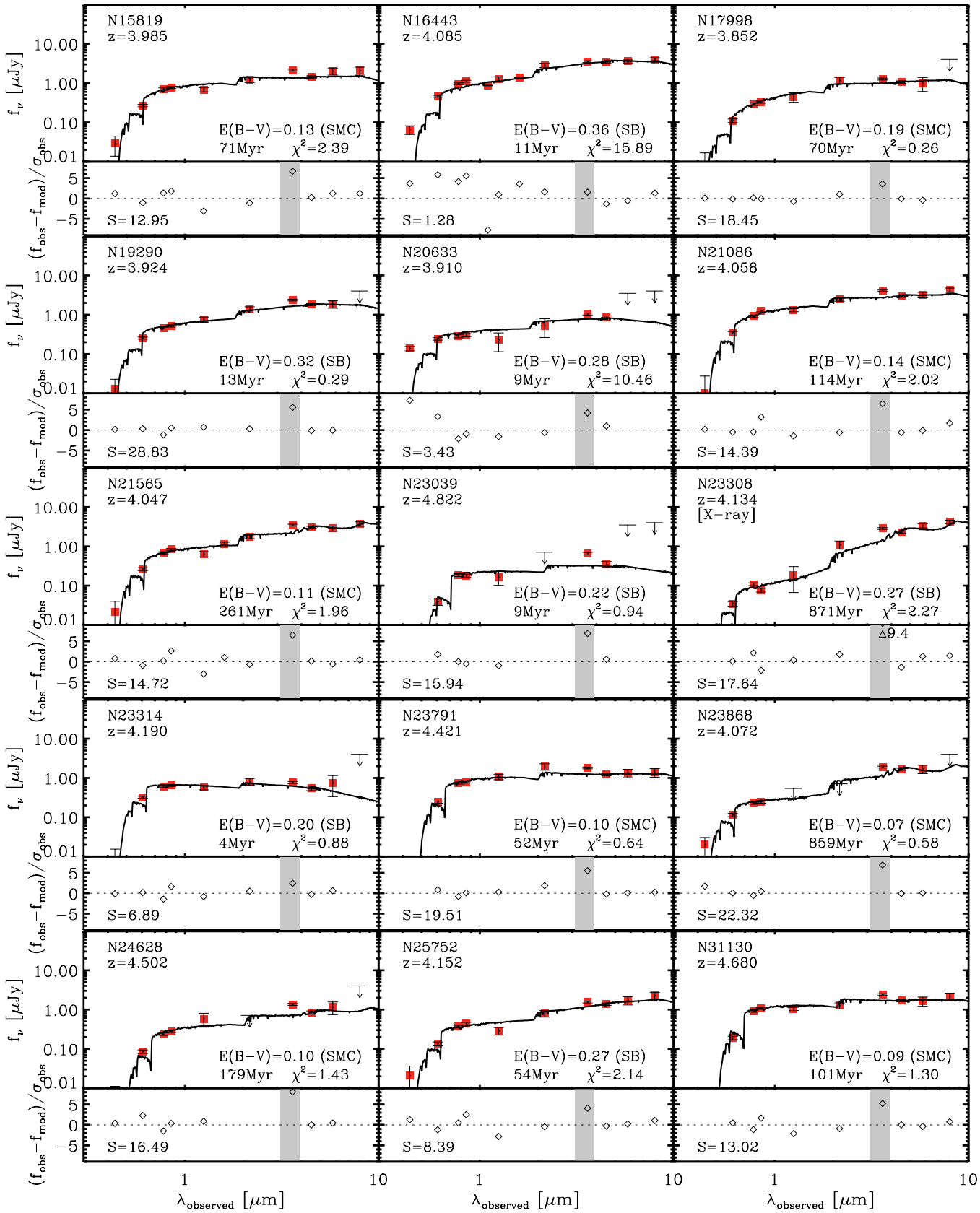

Figure 2. (Continued)

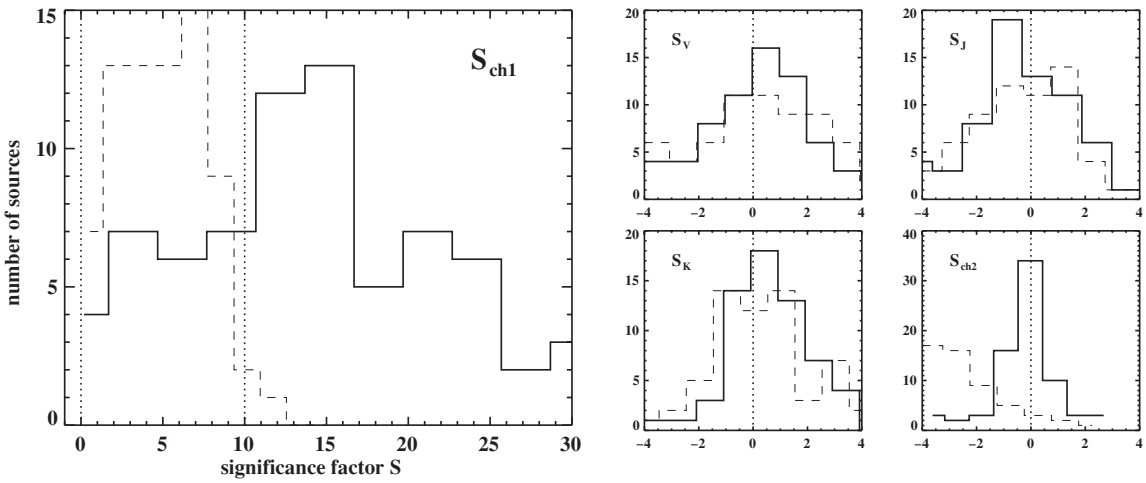

Figure 3. Distribution of "significance factor" S in different filters—IRAC ch1 (3.6 μm), V, J, K, and IRAC ch2 (4.5 μm). The definition of S is given in Section 3.2, Equation (2). The distributions are presented for two different cases: the solid lines show SED fitting without 3.6 μm data and the dashed lines show SED fitting including 3.6 μm data. Unlike the other filters (V, J, K, and 4.5 μm) which show distributions centered around $S = 0$, the $S_{\rm ch1}$ distribution is clearly centered above 0. Even if we try to "fit" the observed 3.6 μm flux (dashed lines), $S_{\rm ch1}$ remains positive and the stellar continuum matched to 3.6 μm overpredicts the 4.5 μm flux (see the lower right panel for $S_{\rm ch2}$ distribution).

quality of the SED fitting. Therefore, the factor $S_{\rm ch1}$ represents the significance of the ch1 excess compared to typical residuals at other wavelengths from the SED fitting.

We show the distribution of the significance factor $S_{\rm ch1}$ in Figure 3. The distribution of factor S in other filters (V, J, K, and IRAC ch2) are also presented for reference. In all but one galaxy, S15920, the factor $S_{\rm ch1}$ is larger than 0. This differs from the other filters, in which the distribution of S is close to a Gaussian distribution with mean value of $S = 0$—confirming that the SED fitting is reasonable. The mean value of $S_{\rm ch1}$ larger than 0 is derived by excluding IRAC ch1 photometry during the SED fitting (solid line in Figure 3); as described above. However even if ch1 photometry is included in the SED fitting (dashed line), the result is the same. The S for other filters is distributed around $S = 0$ while the $S_{\rm ch1}$ is distributed around $\langle S_{\rm ch1}\rangle > 0$, although the mean value $\langle S_{\rm ch1}\rangle$ decreases by a factor of two compared to fits which exclude the ch1 photometry. The $S_{\rm ch2}$ values tend to be negative when ch1 photometry is included in the SED fitting, since the stellar continuum adjusted to match the high ch1 flux overpredicts the ch2 flux. Therefore, it is clear that there exists an excess in 3.6 μm photometry for $3.8 < z < 5.0$ galaxies. Among 74 galaxies, 64 galaxies have "reasonable" SED fitting results, i.e., χ^2 less than 5. All 64 of these galaxies have $S_{\rm ch1}$ greater than 0; thus, we call these 64 galaxies with positive residual in IRAC ch1 "HAE candidates." We classify the subset of 47 galaxies with $S_{\rm ch1} > 10$ as bona fide HAEs. Thus, at least ~65% (47/74) of the spectroscopically confirmed galaxies at $3.8 < z < 5.0$ are found to be HAEs.

The most plausible explanation for the 3.6 μm excess is the addition of the Hα emission line to the stellar continuum. Other possibilities for this excess include the photometric errors produced by uncertainties in the zero-point calibration, the aperture correction, and/or the color correction. The uncertainties in zero-point calibration in IRAC 3.6 μm and 4.5 μm are less than 2% according to the *Spitzer* Data Users' Manual.[8] The uncertainties in aperture correction for IRAC 3.6 μm and 4.5 μm are less than 5%. Moreover, the point-spread function of IRAC 3.6 μm and 4.5 μm are comparable to each other; thus, the aperture correction would be unlikely to cause a systematic flux density increase in IRAC 3.6 μm compared to IRAC 4.5 μm. Finally, the color correction is less than 10% for blackbody spectra of any temperature as well as for most of the galaxy SEDs. Considering all these photometric uncertainties that might affect the 3.6 μm photometry, we conclude that the effects are negligible and 3.6 μm excess should be interpreted as the contribution of Hα emission from these galaxies.

3.3. Estimation of Hα Line Flux and Equivalent Width

The excess in the 3.6 μm photometry compared to the determined stellar continuum from SED fitting is converted into an Hα line flux. We added a Gaussian emission line to the best-fit stellar continuum as a proxy for the Hα emission line, and then increased the amplitude of the Gaussian to determine the Hα line flux that reproduces the observed excess in IRAC 3.6 μm flux density. The width of the Gaussian does not affect the derived line flux, since the line flux is an integral over wavelength. The Hα luminosity derived in this way is the sum of Hα and [N II] doublet at 6583, 6548 Å. In order to correct the derived L(Hα) for [N II] contamination, we assume the relation [N II] $\lambda\lambda$6583/Hα = 0.3 and [N II] $\lambda\lambda$6583/[N II] $\lambda\lambda$6548 = 3 (Gallego et al. 1997). This ratio is obviously metallicity-dependent, yet since we do not have strong evidence constraining the metallicity of HAEs, we use the conventional [N II]/Hα ratio for [N II] correction. The luminosity, the EW, and the flux of Hα line used throughout this paper are all corrected for [N II], using this correction: $f_c(\mathrm{H}\alpha) = 0.71 \times f(\mathrm{H}\alpha + [\mathrm{N\,II}])$.

We present the Hα luminosity and the EW of all (74) galaxies at $3.8 < z < 5.0$ in Table 2. The EWs are the values in the rest-frame. One object (S15920) has $S_{\rm ch1} < 0$ thus its Hα luminosity could not be measured. Among these 74, 64 galaxies are considered to be galaxies with reasonable SED fitting and 47 are considered as significant (bona fide) HAEs as noted in Section 3.2. The derived L(Hα) of all $3.8 < z < 5.0$ galaxies ranges between $10^{42.4} < L_{\rm H\alpha}[\mathrm{erg\,s^{-1}}] < 10^{43.8}$, corresponding to SFRs of 20–500 $M_\odot$ yr^{-1} assuming the SFR calibration of Kennicutt (1998a). Figure 4 (left) shows the luminosity distribution of $z \sim 4$ HAE candidates (64 galaxies, with reliable SED fitting and L(Hα) estimates) and the Hα-inferred SFRs as a function of stellar mass which is derived from the SED fitting. The HAE candidates are found to be very actively

[8] http://ssc.spitzer.caltech.edu/dataanalysistools/cookbook/

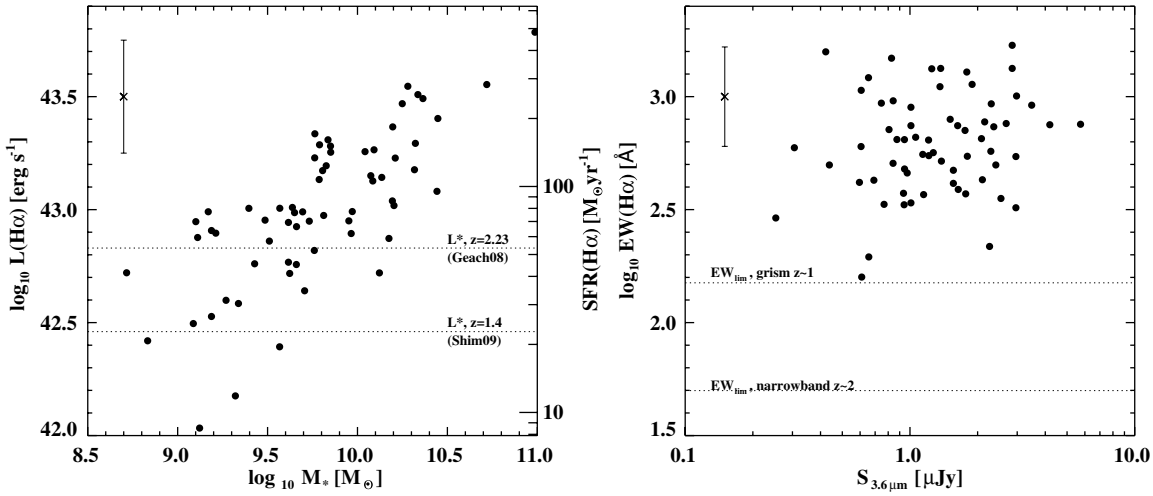

Figure 4. Left: Hα luminosity of $z \sim 4$ HAE candidates as a function of stellar mass. The right axis shows the inferred SFR from the Hα luminosity. The plotted error bar represents the typical uncertainty in Hα luminosity. The horizontal dotted lines indicate $L_{*,\mathrm{H}\alpha}$ at $z = 1.4$ (Shim et al. 2009) and $z = 2.23$ (Geach et al. 2008), respectively. Right: Hα equivalent width of $z \sim 4$ HAE candidates relative to their 3.6 μm flux density. The error bar indicates the typical uncertainty in the derived Hα equivalent width. The horizontal dotted lines indicate the minimum equivalent width that could be detected in other surveys, i.e., grism survey at $z \sim 1$ (Shim et al. 2009) and narrowband imaging survey at $z \sim 2$ (Geach et al. 2008). Clearly, the $z \sim 4$ population shows stronger Hα emission than star-forming galaxies at $z \sim 1$ or $z \sim 2$.

star-forming galaxies: most have Hα emission that is substantially stronger than the characteristic luminosity $L_{*,\mathrm{H}\alpha}$ for galaxies at lower redshifts (e.g., $10^{42.83\pm0.13}$ erg s^{-1} at $z = 2.23$, $10^{42.46\pm0.19}$ erg s^{-1} at $z = 1.4$; Geach et al. 2008; Shim et al. 2009).

In Table 2, the uncertainties in $L_{\mathrm{H}\alpha}$ are presented as well. The major uncertainties in the derived $L_{\mathrm{H}\alpha}$ come from: (1) uncertainties in the photometry at 3.6 μm and (2) uncertainties in the determination of stellar continuum level at 3.6 μm. Since our sample galaxies have relatively high S/N in 3.6 μm (mostly >10), the dominant origin of the uncertainties is the latter. We derive the uncertainties using a Monte Carlo analysis. For each galaxy, 100 sets of multi-band photometry were generated by simulating a Gaussian distribution of flux densities around the measured flux densities. That means, the photometry sets are $[S_B^i, S_V^i, S_I^i, \ldots S_{\mathrm{ch4}}^i]$ with S_{filter}^i being drawn from a Gaussian distribution of flux density values at the given filter which reproduces the photometric uncertainty at that filter. We then re-derive the best-fit stellar continuum through the SED fitting as before and re-estimate the value of $L_{\mathrm{H}\alpha}$. From the distribution of the 100 sets of the derived $L_{\mathrm{H}\alpha}$, we take the standard deviation as the uncertainty in the Hα luminosity. The Hα luminosity uncertainties in Table 2 are derived following this procedure.

3.3.1. Validation of Photometric Estimates

We tested the validity of our EW(Hα) estimates from the broadband photometric excess using galaxies at lower redshifts that have spectroscopic measurements of EW(Hα). The galaxies used in this verification are 15 galaxies at $z \sim 2$ (Erb et al. 2006) with available multi-band photometry at U_n, G, R, J, K, *Spitzer*/IRAC 3.6 μm and 4.5 μm bands (Reddy et al. 2006). These galaxies are vigorous star-forming galaxies selected in the rest-frame UV. The EW(Hα)s of these galaxies are measured to be 70–300 Å, which are comparable with those of our HAE candidates at $z \sim 4$. At $2.1 < z < 2.5$, the Hα emission line is redshifted to ~2.2 μm, causing the flux density excess to be in the K band.

Figure 5 shows the comparison between spectroscopically measured EW ($\mathrm{EW_{spec}}$) and SED-fitting derived EW ($\mathrm{EW_{phot}}$).

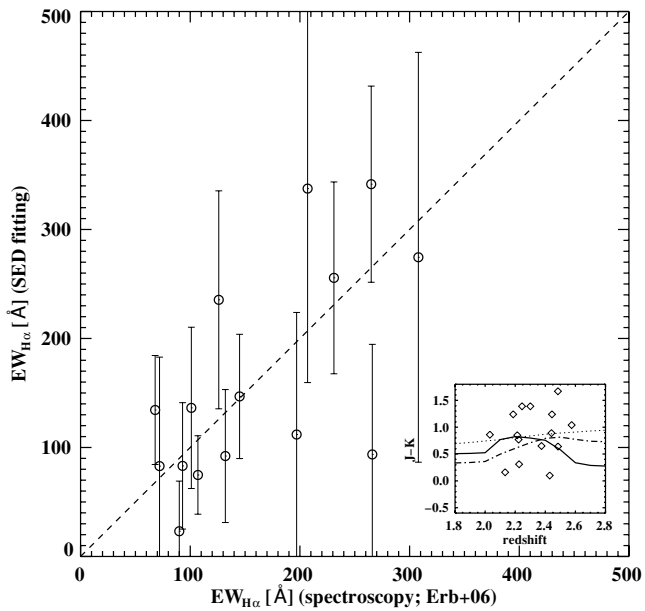

Figure 5. Comparison between Hα equivalent widths derived from broadband photometric excess (y-axis) to equivalent widths measured from observed spectra (x-axis). We consider star-forming galaxies with Hα spectroscopic observations at $2.1 < z < 2.5$ (Erb et al. 2006; Reddy et al. 2006) for this test, assuming that the redshifted Hα emission line is the dominant source of K-band excess. The inset plot shows the K-band excess due to the redshifted Hα line as a function of redshift, where the solid/dot-dashed/dotted lines indicate the expected $J-K$ color for MS1512-cB58/SDSS quasar/reddest galaxy template. The diamonds are the observed $J-K$ colors for $z \sim 2$ star-forming galaxies (Reddy et al. 2006). The correlation between the spectroscopically measured equivalent widths and our photometrically derived values imply that our photometric method is robust.

We used the same method applied to the $z \sim 4$ HAE candidates to derive $\mathrm{EW_{phot}}$, except using K-band excess instead of IRAC ch1 band. The $\mathrm{EW_{phot}}$ reproduces the $\mathrm{EW_{spec}}$ relatively well, within a scatter of ~0.25 dex. There is no significant systematic difference between the two EWs. This validation ensures the reliability of the derived EW(Hα) of the $z \sim 4$ HAE candidates. Almost all of the $z \sim 4$ HAEs have $\mathrm{EW_{phot}}$ larger than 300 Å,

which is the maximum value in the $z \sim 2$ galaxy sample (Erb et al. 2006). The relative accuracy of the Hα line flux measurement from broadband photometry would be better for stronger lines. Therefore, the consistency between EW_{phot} and EW_{spec}, even for weak Hα lines (<300 Å) at $z \sim 2$, supports that this photometric method works for strong lines in $z \sim 4$ HAEs.

There are two objects that show large discrepancies between EW_{spec} and EW_{phot} (one at $EW_{spec} = 90$ Å and the other at 266 Å). Their $J-K$ colors are bluer than the color expected by the star-forming galaxy template (see the inset plot of Figure 5). It appears that the EW discrepancies of these sources are due to large photometric uncertainties in the J and K bands.

3.4. Selection Bias for HAEs from Broadband Photometric Surveys

The HAE candidates are galaxies with large EW(Hα), i.e., EW(Hα) = 140–1700 Å (Table 2; Figure 4 (right)). Since the EW is the ratio between the line luminosity and the continuum luminosity at the wavelength of the emission line, photometric uncertainties in IRAC ch1 place a limit on the detectable EW(Hα). We calculated the minimum EW(Hα) that could be detected using the criterion that an HAE candidate should show IRAC ch1 excess at least three times larger than the uncertainties, including both photometric uncertainty and stellar continuum uncertainty. The EW(Hα) limit varies between 70 and 350 Å for different galaxies (note that these limits are rest-frame EW limits). This limit is relatively large compared to the observational EW limit of narrowband surveys (e.g., Geach et al. 2008; 50 Å), yet comparable to the limit for low-resolution grism surveys (e.g., Shim et al. 2009; 150 Å). This shows that HAE candidates selected using broadband photometric excess are biased toward strong HAEs, comparable to the strongest emission-line galaxies selected in grism surveys.

If the star formation in a galaxy is instantaneous, then such strong Hα emission ($EW_{H\alpha} \gtrsim 100$ Å) is short-lived, lasting for only ~5 Myr after the starburst (Leitherer & Heckman 1995). On the other hand, if the star formation is extended (i.e., continuous star formation), this phase of large Hα EW lasts longer. Considering only instantaneous star formation for galaxies, our redshift window of $3.8 < z < 5.0$ spans ~470 Myr of cosmic time, implying the chance for selecting such HAEs to be only ~1%. The observed fraction of HAEs among spectroscopically selected galaxies at $3.8 < z < 5.0$ is more than an order of magnitude larger than that (47/124), which suggests that the star formation timescale of $z \sim 4$ galaxies appears to be extended, not instantaneous. Note however that due to the fact that the target selection for spectroscopic observation is mostly based on the UV colors (i.e., dropout selection), it is also probable that our sample is biased toward young galaxies with large ongoing SFRs.

4. ORIGIN OF STRONG Hα EMISSION

We have demonstrated that a significant fraction of $z \sim 4$ galaxies show strong Hα emission. The Hα-derived SFR and the UV-derived SFR using the relation in Kennicutt (1998a) suggest a median ratio of $\langle SFR(H\alpha)/SFR(UV)\rangle \sim 6.1$, although with a large scatter of 4.9. The Hα-to-UV luminosity ratio of $z \sim 4$ HAEs is on average larger than that of local starbursts (Figure 6). What could be the origin of such strong Hα emission in these galaxies? In this section, we present several possibilities to explain the strong Hα emission in HAEs.

4.1. The Effect of Dust Extinction

The estimation of the internal reddening for high-redshift galaxies is generally based on the UV spectral slope β, following the work on local starbursts (e.g., Meurer et al. 1999). The method requires the unverified assumption of the similarity in the intrinsic SEDs of local and high-redshift star-forming galaxies as well as a similarity in the dust obscuration properties. The IR luminosity to UV luminosity ratio of $z \sim 2$–3 star-forming galaxies (e.g., Siana et al. 2009; Reddy et al. 2010) have suggested possible discrepancies between dust extinction laws for high-redshift star-forming galaxies and local star-forming galaxies. The ratio between the rest-frame optical emission line and the rest-frame UV continuum provides an independent test for the validity of the assumed similarity between low- and high-redshift star-forming galaxies.

The derived Hα line-to-UV continuum ratio (hereafter line-to-continuum ratio) is compared with UV spectral slope β in Figure 6. The line-to-continuum ratio is not to be confused with an EW since the line flux and continuum are measured at different wavelengths. The number of HAE candidates with reliable SED fitting results ($\chi^2 < 5$) is 64, including one object with an X-ray counterpart (N23308). This object lies out of the range plotted in Figure 6. Though there exists a considerable scatter, the β and the line-to-continuum ratio correlates with a Spearman's coefficient (ρ_s) of 0.52 which is significant at the level of >70%. Also shown are the β versus line-to-continuum ratios for local starburst galaxies, which are taken from Meurer et al. (1999; originally observed by Storchi-Bergmann et al. 1995; McQuade et al. 1995). The $z \sim 4$ HAE candidates lie in clearly different regions of β versus line-to-continuum space compared to local starbursts. This is quantitatively supported by a Kolmogorov–Smirnov test, which shows that the probability of the two groups having the same correlation between the β and line-to-continuum ratio is less than 1%.

In order to assess the origin of this difference, we overplot several model tracks on the observed data points in Figure 6 (left). The model tracks are reddened assuming different extinction laws: the starburst extinction law (Calzetti et al. 2000), the SMC extinction law (Prévot et al. 1984), and the LMC extinction law (Fitzpatrick 1986) without the 2175 Å graphite feature. When each extinction law is applied, different factors are used for the line and the continuum, following the statement in Calzetti (2001) that the stellar continuum suffers roughly half of the dust reddening suffered by the ionized gas due to the mixed dust geometry. Thus, the observed $F_{H\alpha}$ is modulated using $E(B-V)_{gas}$ at the Hα wavelength (6563 Å), defined by $E(B-V)_{star} = 0.44E(B-V)_{gas}$.[9]

The high line-to-continuum ratio is reproduced by young galaxies with long star formation timescales. With the same e-folding time τ for star formation, there is a factor of three difference in line-to-continuum ratio between galaxies of 1 Myr age and 10 Myr age. For the same age of 100 Myr old, there is a factor of 2.5 difference in line-to-continuum ratio between instantaneous starburst galaxies and continuously star-forming galaxies. In addition, different extinction laws produce differences in line-to-continuum ratio. The SMC/LMC extinction laws have slightly steeper β versus line-to-continuum relations than the SB extinction law. The slope is 0.24 and 0.27 for SMC and LMC extinction laws, respectively, and is 0.18 for the SB

[9] There exist controversy on the value of the factor $E(B-V)_{star}/E(B-V)_{gas}$, from 0.44 (Calzetti 2001) to ~1 (Reddy et al. 2010).

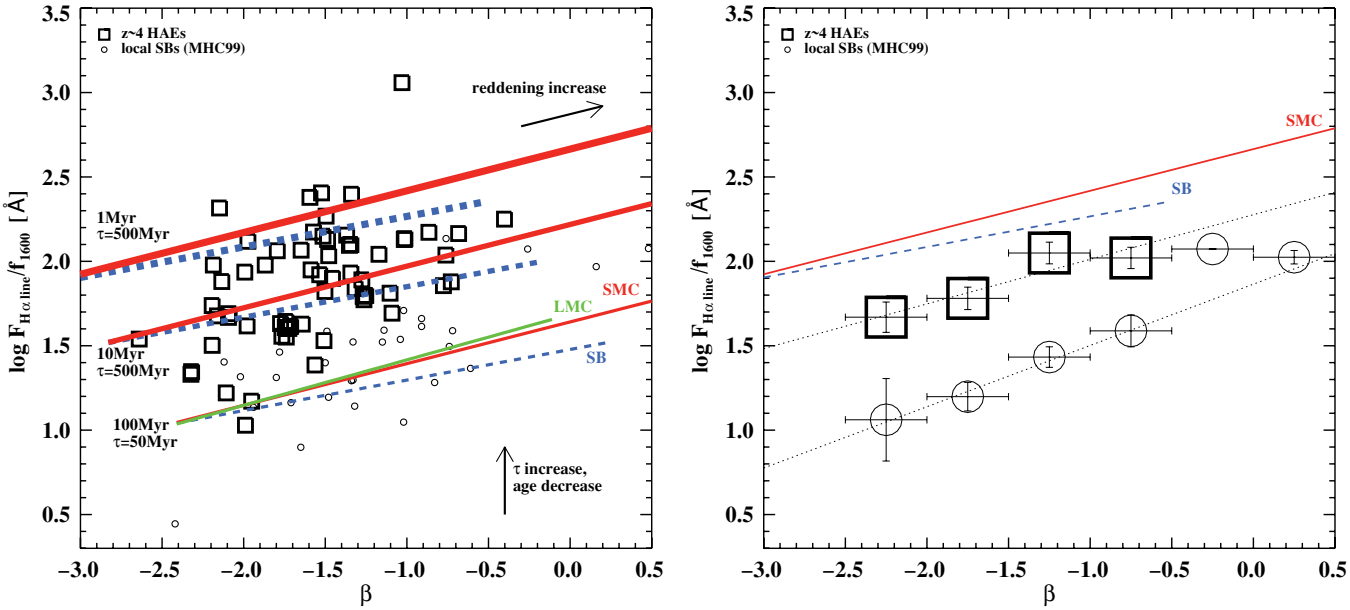

Figure 6. Left: comparison between two different extinction measures, UV spectral slope β and the Hα line flux to UV flux ratio. All (64) HAE candidates are plotted (squares). The circles indicate local starburst galaxies (data originally published by Storchi-Bergmann et al. 1995 and McQuade et al. 1995; taken from Meurer et al. 1999). The overplotted lines show the relation between β and $f_{\rm H\alpha}/f_{1600}$ for different extinction laws and stellar population synthesis models. The solid, dashed, and dot-dashed lines show the SMC (Prévot et al. 1984), SB (Calzetti et al. 2000), and LMC (Fitzpatrick 1986) extinction laws without the 2175 Å graphite feature, respectively. The relation moves upward when the galaxy is younger and the star formation history is more extended. Right: comparison between β vs. line-to-continuum ratio for local starbursts, HAE candidates, and SB/SMC extinction laws. The symbols represent mean $f_{\rm H\alpha}/f_{1600}$ values in bins of 0.5 in β (squares for HAE candidates, circles for local starbursts). The error bars are derived through bootstrapping, and the lines are the best-fitted linear fits to the points. The slope of the lines are 0.18, 0.24, and 0.26 for SB, SMC, and LMC extinction laws. The slope of the β vs. line-to-continuum ratio for $z \sim 4$ HAEs is 0.27 ± 0.07. Thus, although the HAEs appear to prefer the SMC or LMC extinction law, the derived slope is only different by 1.5σ compared to the SB extinction law.

(A color version of this figure is available in the online journal.)

extinction law. Figure 6 (right) compares the β versus line-to-continuum ratio for local starbursts and HAE candidates with those expected by the SMC and SB extinction laws. The slope in β versus line-to-continuum ratio for $z \sim 4$ HAE candidates is 0.27 ± 0.07. This indicates that the steeper shape of the extinction curve with decreasing wavelength that is found in the SMC/LMC describes the high line-to-continuum ratio observed in $z \sim 4$ HAE candidates marginally better. Thus, it is clear that HAE candidates prefer the SMC extinction law than the SB extinction law while the slope uncertainty is greater than the slope difference between the SMC and SB extinction laws. We note that the relation between line-to-continuum ratios and β of local starbursts is also closer to SMC extinction law than SB extinction law, which is already mentioned in Meurer et al. (1999) yet the reason is not clearly understood.

4.2. The Effect of Age

Other dominant factors that affect Hα EWs are the stellar population age and the star formation timescale. For galaxies with brief bursts of star formation, the EW(Hα) drops to 1% of the initial value (ranging between 1600 and 3200 Å depending on the metallicity) after ~10 Myr (Leitherer et al. 1999). For galaxies with constant star formation, EW(Hα) decreases to 10% of the initial value (ranging between 1800 and 3200 Å depending on the metallicity) after ~100 Myr.

Figure 7 shows a comparison between the derived Hα EW and the age of the stellar population compared to population synthesis models of the EW for different star formation histories. If the derived ages are assumed to be reliable, we find that even though the observed EW(Hα) of 140–1700 Å can be easily reproduced by young and continuously star-forming galaxies, the stellar population in the $z \sim 4$ galaxies are quite heterogeneous; the minority are bursty and younger than ~10 Myr old while the majority are extended with an e-folding timescale of star formation which is comparable to the Hubble time at their redshift. A comparison with the $z \sim 2$ galaxies which are shown in the plot reveals that a larger fraction of $z \sim 4$ galaxies (40%) show burst-like star formation histories compared to the $z \sim 2$ galaxies (7%). We note that the $z \sim 2$ galaxies were fit with extended star formation histories (Erb et al. 2006) which tends to result in larger ages and a smaller burst fraction. However, when we fit the $z \sim 4$ HAEs with only extended star formation histories, we still get a larger fraction of galaxies with burst-like star formation histories at $z \sim 4$.

4.3. The Effect of IMF and Metallicity

Another factor that affects the EW(Hα) is the stellar IMF. A top-heavy IMF implies more early-type stars that dominate the Lyman continuum and thereby Hα production. By changing the power-law slope for the IMF ($N(M) \propto M^{-\alpha}$) from 2.3 to 2.0, 1.7, and 1.5, there is 3%, 8%, and 16% increase in the EW(Hα), respectively, when the stellar population age is the same and the star formation is described as a single burst (Starburst99; Leitherer et al. 1999). If the star formation is assumed to be continuous with a constant rate of 10 $M_\odot$ yr^{-1}, the change of power-law slope from 2.3 to 2.0, 1.7, 1.5, and 1.3 results in an increase of the EW(Hα) of 47%, 110%, 250%, and 290% at the stellar population age of 100 Myr old.

Metallicity also affects EW(Hα), especially when the stellar population age gets older compared to star-forming timescale. For example, the EW(Hα) ratios of 0.02 $Z_\odot$ and 0.2 $Z_\odot$ galaxy to $Z_\odot$ galaxy are 1.18 and 1.12 when the galaxy is 1 Myr old

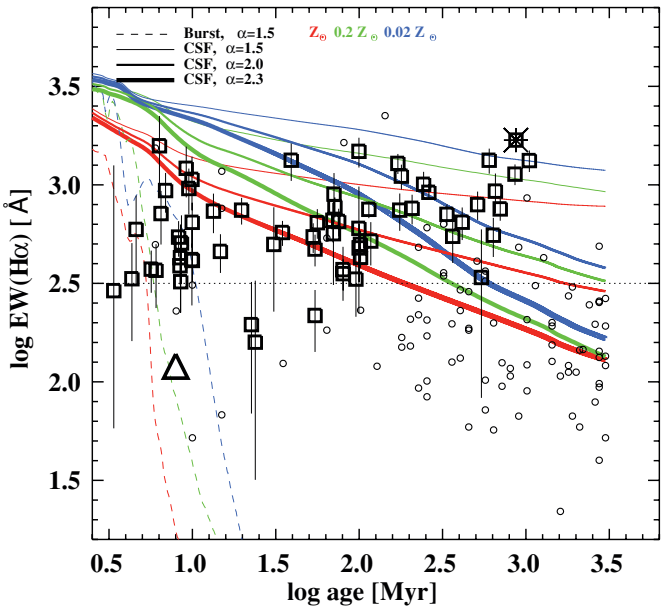

Figure 7. Relation between the estimated EW(Hα) and the stellar population age from the SED fitting. All (64) HAE candidates are plotted as squares, the asterisk is N23308, an object with an X-ray counterpart, probably an AGN. Overplotted are $z \sim 2$ star-forming galaxies selected in the UV (circles; Erb et al. 2006), MS1512-cB58, a gravitationally lensed LBG at $z = 2.72$ (triangle; Teplitz et al. 2004; Siana et al. 2008). The horizontal dotted line at log EW(Hα) ~ 2.5 is the median EW limit for galaxies that could be identified as HAEs using photometric excess in the 3.6 μm band (see the text for details). We overplot the expected EW(Hα) vs. age tracks of models with different star formation history, metallicity, and IMF using STARBURST99 (Leitherer et al. 1999). The dashed lines indicate galaxies that passively evolve after a single burst of star formation, and the solid lines indicate galaxies that constantly produce stars at a rate of 30 $M_\odot$ yr^{-1}. The color of the line indicates the metallicity ($Z_\odot$, 0.2 $Z_\odot$, and 0.02 $Z_\odot$ for red, green, and blue lines). The thickness of the line indicates the slope of the stellar initial mass function α, i.e., $n(M) \propto M^{-\alpha}$. The majority of sources are consistent with an extended star-formation timescale. Some of the highest EWs can be explained with a top-heavy IMF, low metallicity model.

(A color version of this figure is available in the online journal.)

after a single burst. The ratios increase to be 1.9 and 1.6 when the galaxy is 10 Myr old.

It is difficult to assess whether the top-heavy IMF and/or metal-poor metallicity is the origin of large EW(Hα) for the $z \sim 4$ HAEs. Figure 7 shows that the EW(Hα) for galaxies at two different redshifts ($z \sim 2$ and $z \sim 4$) are consistent when the stellar population is less than 100 Myr old. Yet above 100 Myr old, the EW(Hα) is clearly larger for $z \sim 4$ galaxies compared to $z \sim 2$ galaxies with the same stellar population age. If the IMF and metallicity were the dominant factors that affected EW(Hα), this comparison suggests that the metallicity is lower and the IMF is more top-heavy at $z \sim 4$ compared to at $z \sim 2$, at least for the systems with the largest derived EW(Hα).

4.4. AGN Contamination

A fourth possibility is contribution to the Hα emission from an active galactic nucleus (AGN). We matched our HAE candidates to the deep X-ray imaging catalog from *Chandra* (Alexander et al. 2003; Luo et al. 2008) to identify possible AGNs. The sensitivity limit of the X-ray images are $\sim 1.9 \times 10^{-17}$ and $\sim 1.3 \times 10^{-16}$ erg cm^{-2} s^{-1} for the 0.5–2.0 and 2.0–8.0 keV bands in GOODS-South (Luo et al. 2008). The corresponding limits in GOODS-North are $\sim 2.5 \times 10^{-17}$ and $\sim 1.4 \times 10^{-16}$ erg cm^{-2} s^{-1} (Alexander et al. 2003).

Two sources in GOODS-South (S14602, S23763) and two sources in GOODS-North (N12074, N23308) are identified as known X-ray sources using the matching radius of 3″. The X-ray luminosities of the matched objects are 5.3×10^{42}–2.1×10^{43} erg s^{-1} at rest-frame energies of 2.7–10.8 keV at median redshift of $z \sim 4.4$. After the matching, we checked the optical and X-ray images to ensure that X-ray emission is truly from our sources, not from neighboring objects. We calculated the X-ray to optical luminosity ratios for these objects using the X-ray luminosity at rest-frame 2 keV and the optical luminosity at rest-frame 2500 Å. The resultant $F_X/F_{\rm opt}$ ratios for four X-ray detected objects are 0.038–0.073. This is consistent with previously known $z > 4$ quasars detected at X-ray energies (Kaspi et al. 2000). Therefore, these four objects are expected to be powered by AGNs. The relatively poor SED fitting results ($\chi^2 > 5$) of these objects, except for one object (N23308), also support the idea that these are AGNs. Note that N12074 is likely to have an erroneous spectroscopic redshift (see caption in Table 1 and Figure 2), and S14602 is detected at 850 μm (Coppin et al. 2009), which suggests it may harbor an AGN but may be starburst-dominated. In SED fitting, this object does not show photometric excess at 3.6 μm.

We stacked the objects that are not directly detected in the X-ray images following the procedure of Alexander et al. (2003). The stacking yields non-detections in both fields, i.e., $S_{0.5-2\,\rm keV} \lesssim 3\sigma$ flux limits of $\sim 3.0 \times 10^{-18}$ and $\sim 2.0 \times 10^{-17}$ erg cm^{-2} s^{-1} for GOODS-South and $\sim 5.5 \times 10^{-18}$ and $\sim 3.7 \times 10^{-17}$ erg cm^{-2} s^{-1} for GOODS-North, respectively. At $z \sim 4$, this upper limit in X-ray flux corresponds to a luminosity limit of $< (5.3$–$9.5) \times 10^{41}$ erg s^{-1} at rest-frame energies of 2.5–10 keV and $< (3.4$–$6.5) \times 10^{42}$ erg s^{-1} at rest-frame energies of 10–40 keV. We calculated the $F_X/F_{\rm opt}$ ratios using the same method as above, and the result is $F_X/F_{\rm opt} \lesssim 0.011$ at $z \sim 4$. This value is smaller by a factor of > 3 compared to the objects with individual detection in X-ray. Assuming that the $F_X/F_{\rm opt}$ ratio is not dependent on the optical luminosity, as suggested in previous studies (Kaspi et al. 2000; Brandt et al. 2006), this low $F_X/F_{\rm opt}$ ratio for our sources rule out the possibility of strong AGN contamination in sources not directly detected at X-ray energies. According to the number of matched objects to the X-ray catalog and the non-detection in the X-ray stacked images, the AGN fraction among HAE candidates is $\sim$5%. Thus, AGNs can be ruled out as the origin of strong Hα emission in these galaxies.

5. STAR FORMATION AND MASS ASSEMBLY SINCE $z \sim 4$

As described in Section 3.4, HAE candidates have a rest-frame Hα EW of 140–1700 Å, indicating large current SFRs compared to that derived from the UV continuum. In this section, we investigate the dominant mode of star formation in these HAEs, and the implications for the build up of massive galaxies at $z \sim 2$–3.

5.1. Extended versus Bursty Star Formation

Since the most dominant factors that drive large EW(Hα) are stellar population age and star formation history (Leitherer & Heckman 1995; see Section 4.2), we investigate the correlation between age and EW(Hα) for the 64 HAE candidates (Figure 7). The overplotted lines in Figure 7 are the expected EW(Hα) versus age tracks as a function of star formation history, metallicity, and IMF (Starburst99; Leitherer et al. 1999). Other

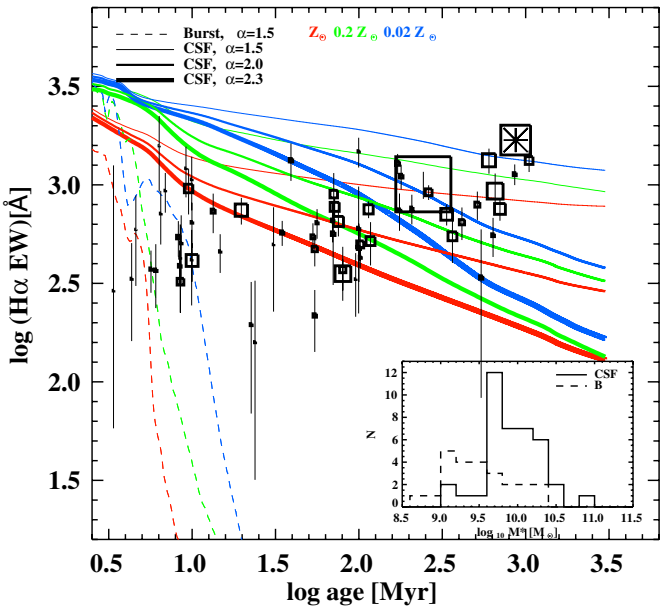

Figure 8. Relation between the estimated EW(Hα) and the stellar population age as a function of galaxy stellar mass. Model tracks are the same as in Figure 7, and the asterisk again indicates N23308 as noted in Figure 7. The symbol size is proportional to the stellar mass. Galaxies older than 30 Myr are classified as those that prefer continuous star formation due to their large EW(Hα) for their evolved ages. The inset plot shows the stellar mass distribution of galaxies that have different star formation histories. The solid histogram is the stellar mass distribution of the 39 galaxies that prefer "continuous star formation." The dashed histogram is the stellar mass distribution of the 24 galaxies that prefer "instantaneous bursts"; i.e., are younger than 30 Myr. The median stellar masses are $\langle M_*\rangle = 7.1\times10^9\ M_\odot$ and $\langle M_*\rangle = 3.1\times10^9\ M_\odot$ for continuous star formation and instantaneous burst, respectively. Lower mass galaxies appear to show bursty star formation histories.

(A color version of this figure is available in the online journal.)

than the one likely AGN (asterisk; see Section 4.4), all 63 objects lie over the tracks suggested by the models: 24 (~40%) are consistent with the instantaneous burst models and the remaining 39 (~60%) are consistent with the continuous star formation models. This is based on the stellar population age derived using SED fitting assuming a fixed metallicity of 0.2 $Z_\odot$ for galaxies. If these galaxies are more metal-rich, their stellar population age would be even lower. The metallicity cannot be verified with current data and so we adopt the low metallicity assumption that is common for high-redshift galaxies. According to the model tracks, the large EW(Hα) implies one or more of the following for the HAEs: (1) the galaxy is young, (2) the galaxy is more likely to form stars continuously than instantaneously, (3) the galaxy is relatively metal-poor, and/or (4) the IMF is top-heavy.

We use the derived age to divide the HAEs into two groups: 24 galaxies that prefer instantaneous star formation (ages <30 Myr) and 39 galaxies that prefer continuous star formation (ages >30 Myr). We find that 60% of HAE candidates prefer "extended" star formation rather than "bursty" star formation, indicating that more than half of the $z\sim4$ galaxies are forming stars at a relatively constant rate. In order to investigate the factors that yield the different star formation histories among $z\sim4$ HAE candidates, we compare the stellar masses and morphologies of HAE candidates in the age versus EW(Hα) plot. Figure 8 shows the age versus EW(Hα) relation as a function of stellar mass, with the symbol size proportional to the stellar mass. There is a factor of two difference between the mean stellar mass of the two populations: $\log M_*\,(M_\odot) = 9.85\pm0.36$ for continuous star-forming galaxies and $\log M_*\,(M_\odot) = 9.49\pm0.44$ for instantaneous burst galaxies. The mean stellar mass for galaxies with continuous star formation is slightly larger than that of galaxies with instantaneous bursts, but it should be noted that the factor of two difference is within the stellar mass uncertainty inferred by SED fitting itself. Note that there are several galaxies with extremely large EW(Hα) which is only reproduced with an extremely metal-poor stellar population and/or a top-heavy IMF. For example, S1478 has a large stellar mass ($M_* = 10^{11} M_\odot$) in addition to a large EW(Hα) and an old stellar population age. It is plausible that such galaxies may harbor AGNs, whose X-ray luminosity is not large or is heavily obscured.

As shown in Figures 9 and 10, galaxies with "extended" and "bursty" star formation are not distinguished in terms of morphologies. We visually divide mergers and non-mergers in the two groups: while 13 of the 24 (54%) instantaneous burst galaxies are apparent merging/interacting systems, 19 of the 39 (49%) continuously star-forming galaxies are classified as merging/interacting systems.[10] The fraction of mergers is roughly half in both cases, which shows that morphology alone, especially in the rest-frame UV, is not enough to describe or represent the star formation mode in galaxies.

Figure 7 also shows that the mode of star formation in $z\sim4$ HAE candidates is different compared to that of star-forming galaxies at lower redshifts. The lensed $z = 2.72$ LBG MS1512-cB58 is well described by the instantaneous burst model (~10 Myr old, Siana et al. 2008; EW(Hα) ~ 100 Å, Teplitz et al. 2004). This supports evidence showing that star formation in sub-L^* galaxies at $z\sim3$ is bursty. On the other hand, $z\sim2$ star-forming galaxies selected in the UV (Erb et al. 2006) clearly occupy the region sampled by the continuous star formation models. As mentioned in Section 4.2, the fraction of galaxies with extended star formation increases from 60% at $z\sim4$ to 93% at $z\sim2$. The difference partly results from the fact that the stellar population ages of $z\sim2$ galaxies are basically derived using constant star formation history models (i.e., $\tau=\infty$; Erb et al. 2006). The choice of τ does affect the derived stellar population ages, by increasing the derived age if τ increases. We test whether the use of constant star formation history models would change the "young" ages (<30 Myr) of ~40% of $z\sim4$ HAEs; we find that most of the galaxies would still be fitted with ages less than 50 Myr even for $\tau=\infty$. Therefore, despite the difference in the star formation history of the stellar population models used in SED fitting, the fraction of continuously star-forming galaxies appears to have significantly increased by $z\sim2$ compared to at $z\sim4$.

5.2. Number Density of HAEs and Massive Galaxies

The HAE candidates with star formation histories best fit by a continuous starburst model have a median stellar age of 80 Myr and a median stellar mass of $7.1\times10^9\ M_\odot$. Therefore, their past average SFR is ~90 $M_\odot$ yr^{-1}, while the current SFR is observed to be in the range of 30–600 $M_\odot$ yr^{-1}. The current SFRs are comparable or even larger than the past value. Assuming that the extended star-formation timescale is due to a steady supply of cold gas, if the HAEs continue to form stars at the measured rate, the HAEs are likely progenitors of massive galaxies at $z = 2$–3.

[10] We have verified the classification of merging and non-interacting systems using the CANDELS WFC3 data in GOODS-South and find the fraction of systems in those two categories to be consistent with that presented here.

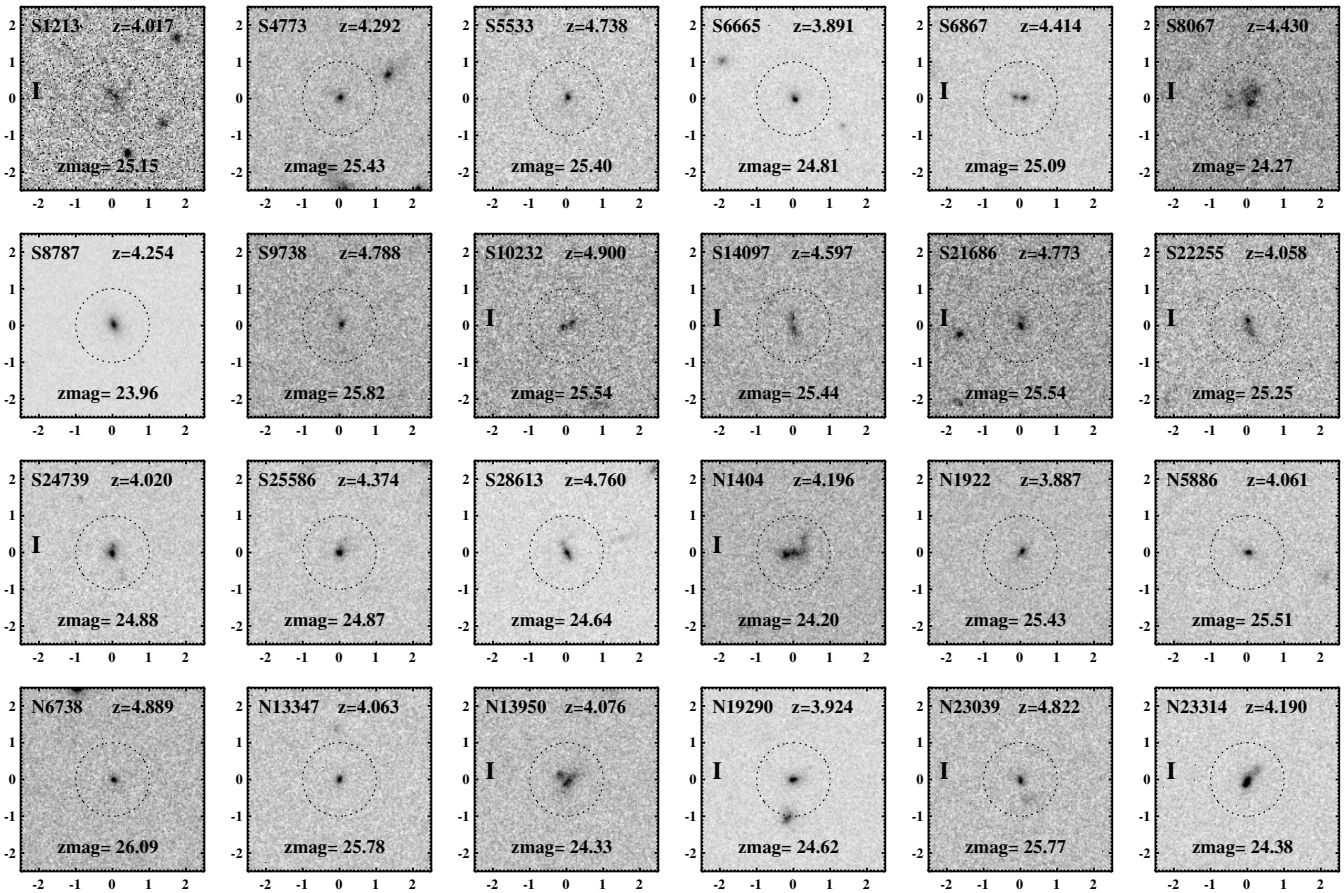

Figure 9. Morphologies of the $z \sim 4$ HAE candidates that have a star formation history corresponding to the instantaneous burst model. The star formation mode classification ("instantaneous" or "continuous") is based on the relationship between the Hα EW and the stellar age (Figure 7): we have classified galaxies older than 30 Myr as galaxies with "continuous" star formation and others as galaxies with "instantaneous" star formation. The postage stamp images are $5'' \times 5''$ cutouts of *HST*/ACS z-band images, e.g., these are rest-frame FUV images at $z \sim 4$. The galaxy ID, spectroscopic redshift, and z-band magnitude are indicated. We mark clearly merging/interacting systems with an "I" in the left of each postage image. Among 24 galaxies, 13 galaxies are classified as clear merging/interacting systems.

As we detect 39 robust HAE candidates having extended star formation timescales (e.g., best fit with continuous star formation), the lower limit on the number density of galaxies that could evolve into massive galaxies at $z = 2$–3 is 3.3×10^{-5} Mpc^{-3}. This is more than 190 times the number density of $z \sim 4$ SMGs discovered so far (Coppin et al. 2009) while the SMGs are considered likely progenitors for massive galaxies due to their large SFRs. The stellar mass density produced by HAEs is calculated by dividing the integral of their SFRs by the survey volume, i.e.,

$$(1/V) \sum_{i}^{\text{galaxy}} \int_{0}^{t_{z_0}} \text{SFR}_i(t)\, dt.$$

The resultant stellar mass density the HAEs can contribute by $z_0 = 2$ and $z_0 = 3$ is $1.1 \times 10^7\, M_\odot$ Mpc^{-3} and $4.4 \times 10^6\, M_\odot$ Mpc^{-3}, respectively, when SFR(t) is fixed to the current observed SFR of each galaxy. Note that this is a lower limit produced by active star-forming galaxies at $z \sim 4$, since our selection of HAE candidates is incomplete due to the limitations of spectroscopic sample incompleteness, IRAC sensitivity limit, and source photometry contamination.

The estimated mass density produced by HAE candidates is 15%–20% of the average global stellar mass density at $z = 2$ and $z = 3$ (Figure 11). The estimated stellar mass of individual HAEs is larger than $10^{11}\, M_\odot$ at $z = 2$ and $5 \times 10^{10}\, M_\odot$ at z=3. Therefore, when compared with the stellar mass density of massive ($M_* > 10^{11}\, M_\odot$) galaxies only, the values are ∼80% and ∼50% of the stellar mass density at $z = 2$ and $z = 3$, respectively. This result suggests that $z \sim 4$ HAE candidates may produce at least 50%–80% of massive galaxies at $z = 2$–3. At $z = 3$, this is ∼5 times higher than the value provided by $z \sim 4$ SMGs (10%, Coppin et al. 2009), which are characterized as an ultraluminous star formation phase for a short duty cycle of ∼100 Myr. Considering that our HAE selection is still incomplete, HAEs can likely account for most of the massive galaxies at $z = 3$. That is, most of the massive galaxies at $z = 3$ apparently are formed through steady, extended star formation rather than through the violent, burst-like star formation frequently reported in mergers.

5.3. Star Formation Rates versus Stellar Mass

The SFRs of HAE candidates are correlated with their stellar masses (Figure 12), similar to the tight correlation between the SFR and the stellar mass of star-forming galaxies at lower redshifts (Elbaz et al. 2007; Noeske et al. 2007; Daddi et al. 2007). The correlation between SFR versus stellar mass of $z \sim 4$ HAEs is significant with a Pearson correlation coefficient of $r = 0.77$. Considering the stellar mass is roughly proportional to the halo mass, and to the gas mass, the tight SFR–M_* correlation is another reflection of Schmidt–Kennicutt law (Schmidt 1959; Kennicutt 1998b) that connects gas density and SFR density.

The SFR–M_* correlation evolves as a function of redshift with the same slope. This may indicate a difference in star

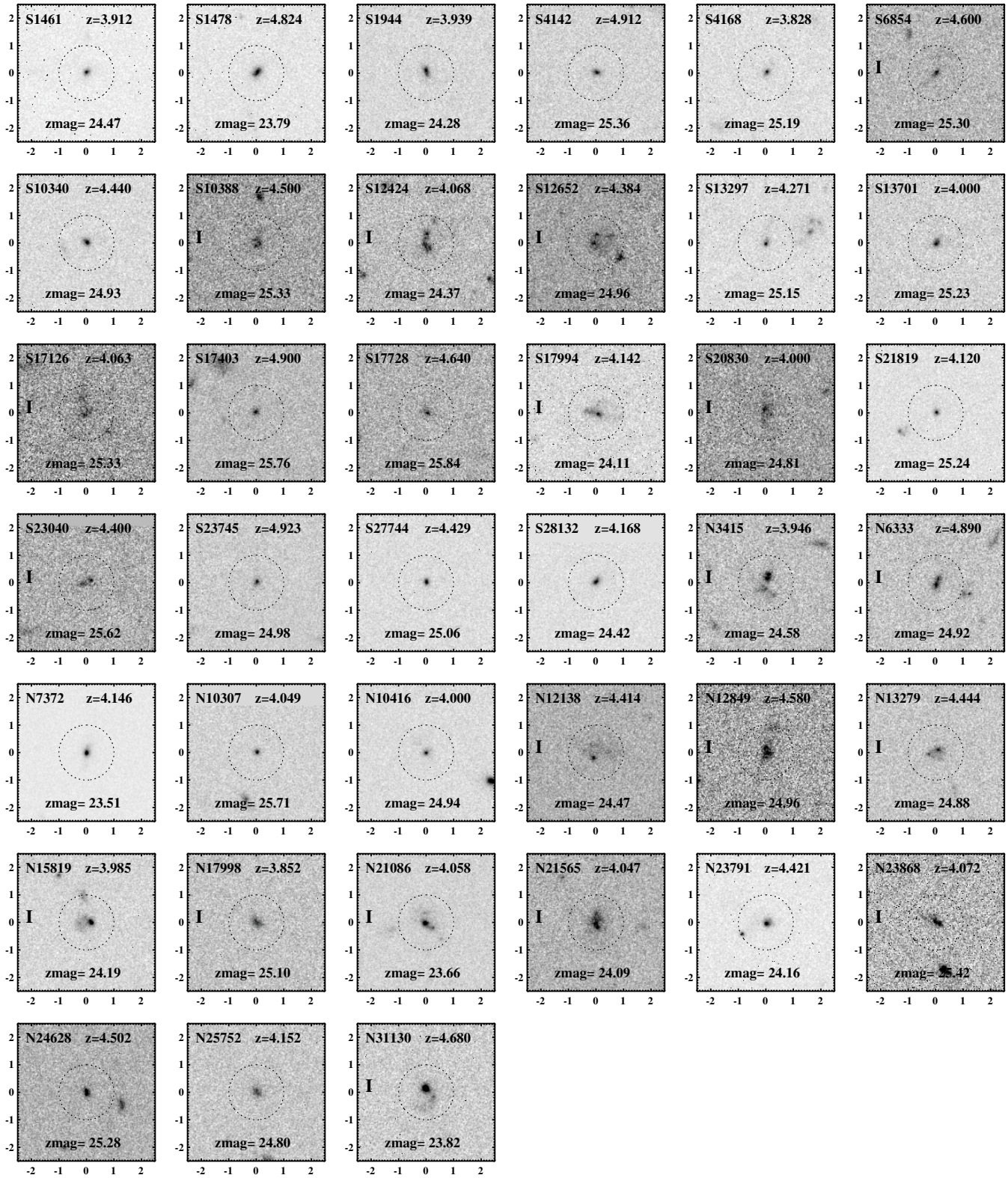

Figure 10. Morphologies of the $z \sim 4$ HAE candidates that have a star formation history corresponding to the continuous star formation model. The images are $5'' \times 5''$ cutouts of *HST*/ACS z-band images as in Figure 9. The galaxy ID, spectroscopic redshift, z-band magnitude, and whether the object is a merging/interacting system or not are marked as in Figure 9. Among 39 galaxies, 19 galaxies are classified as clearly merging/interacting systems.

formation efficiency between galaxies at different redshifts. The big difference between $z \sim 4$ HAE candidates and star-forming galaxies at other redshifts is the comparison with SMGs at similar redshifts. At $z \sim 2$, SMGs are found to be significant outliers in the SFR–M_* relation (Daddi et al. 2009), with SFR a factor of 10 larger than normal star-forming galaxies. The discrepancy implies that star formation efficiency (or gas fraction) is higher in SMGs compared to normal star-forming galaxies at that epoch, which is very likely considering SMGs are wet mergers. On the other hand, known $z \sim 4$ SMGs are located close to the extension of SFR–M_* relation of $z \sim 4$ HAE candidates. We interpret this as the high star formation efficiency (or high

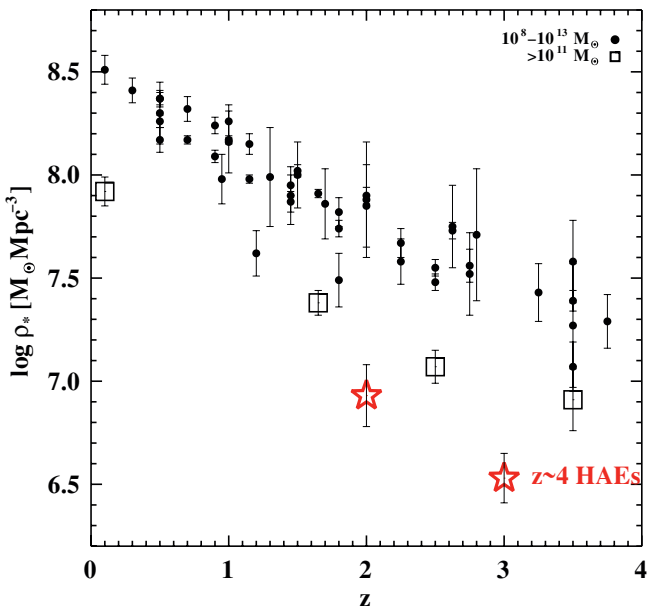

Figure 11. Evolution of stellar mass density as a function of redshift. The points are from the compilation of Marchesini et al. (2009): filled circles indicate the mass density of galaxies with stellar mass of 10^8–10^{13} $M_\odot$, open squares indicate the contribution to the mass density from massive (>10^{11} $M_\odot$) galaxies. The stars are the "expected" mass density that $z \sim 4$ HAEs can harbor at lower redshifts if the HAEs continue to form stars at the SFRs they are observed to exhibit at $z \sim 4$.

(A color version of this figure is available in the online journal.)

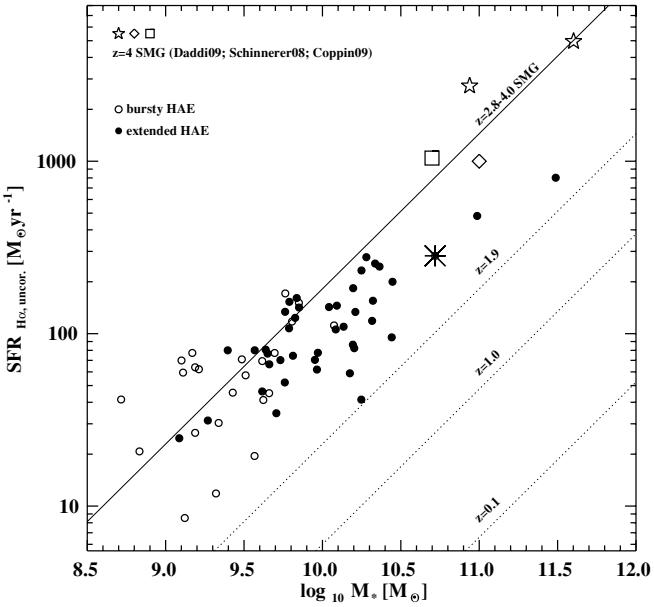

Figure 12. SFR vs. stellar mass correlation for HAE candidates (circles). Galaxies that prefer continuous star formation models are marked as filled circles, and galaxies that prefer instantaneous burst models are marked as open circles. The asterisk indicates N23308, an X-ray-detected AGN. The SFR is derived using the derived Hα line luminosity, and no correction for dust extinction is applied. Also plotted with different symbols are SFR and stellar mass of $z \sim 4$ SMGs (stars from Daddi et al. 2009; diamond from Schinnerer et al. 2008; square from Coppin et al. 2009). The SFR and the stellar mass compared here are based on the assumption of Salpeter initial mass function (Salpeter 1955). The dotted lines are the SFR vs. stellar mass correlation for star-forming galaxies at lower redshifts, $z = 0.1$ for Elbaz et al. (2007), $z = 1.0$ for Noeske et al. (2007), and $z = 1.9$ for Daddi et al. (2007). The solid line indicates the SFR vs. stellar mass correlation of SMGs at $z \sim 2$–4 (Daddi et al. 2009). $z \sim 4$ HAEs show SFR efficiencies similar to merger-driven SMGs, which is surprising, because the HAEs appear to show extended star formation timescales. This suggests that HAEs harbor similar gas surface densities as SMGs.

gas density) of $z \sim 4$ HAE candidates. The morphologies of HAE candidates are not dominated by merging systems; thus, other mechanisms are required to explain the high star formation efficiency and large SFR for HAE candidates. The cold accretion flow scenario can explain the observed number density of HAE candidates that produce SFR larger than 200 $M_\odot$ yr^{-1} (Dekel et al. 2009). Yet the contribution and the importance of merger-induced star formation at this redshift range is difficult to constrain and it is difficult to classify merging systems and non-merging systems based on UV morphologies alone.

6. PREDICTIONS FOR FUTURE OBSERVATIONS

The expected Hα line flux of HAEs is 10^{-17}–10^{-16} erg s^{-1} cm^{-2}, which indicates that the HAEs presented in this paper are potential targets for the *James Webb Space Telescope* (*JWST*) to confirm and measure the strength of Hα emission at $z > 4$ for the first time. With the expected line flux and the observed 4.5 μm continuum level of 23–25 mag(AB), we expect to get S/N of ~10 for the emission line and S/N ~ 3 for the continuum with an exposure of 1200–1800 s using the G395($R \sim 1000$)/F290LP grating/filter setting of *JWST*/NIRSPEC.[11]

We have discussed different scenarios for the origin of such strong Hα emission in the previous sections. If the large Hα EWs are due to dust obscuration, we calculate the range of the intrinsic SFR of the HAEs is 20–500 $M_\odot$ yr^{-1}, corresponding to an infrared luminosities of $\lesssim 2 \times 10^{12}$ $L_\odot$. We calculated the expected far-infrared/millimeter fluxes for the HAE candidates using the derived SFR(Hα) and checked whether these objects are detectable in future surveys at long wavelengths. The $L_{\rm IR}$ of the HAE candidates derived from SFR(Hα) ranges from 1.2×10^{11} $L_\odot$ to 2.3×10^{13} $L_\odot$. This is consistent with the $L_{\rm IR}$ calculated using the difference between the best-fit template and its unattenuated form, with a scatter of ~0.5 dex.

Figure 13 shows the IR templates that represent $L_{\rm IR}$ of each object at its observed redshift. The IR templates are from Chary & Pope (2010). The observed optical-to-MIR fluxes are overplotted as circles and lines that connect the circles. At wavelengths longward of 70 μm, the HAE candidates show a wide range of flux densities. The limits for current and future space- and ground-based missions are indicated as horizontal shaded region: blue for the Herschel/Photodetector Array Camera and Spectrometer limits (PACS; GOODS-Herschel program), green for the Herschel/Spectral and Photometric Imaging REceiver limits (SPIRE; GOODS-Herschel), and red for the expected sensitivities of the Atacama Large Millimeter/Submillimeter Array (ALMA). Assuming that these IR SEDs are valid for HAE candidates, we expect to detect ~10% of HAE candidates using GOODS-Herschel data, primarily by SPIRE. Our candidates are relatively free of source confusion, at least on scales of a few arcseconds, due to their selection in IRAC images. However, the SPIRE beam size of 15″–20″ is still too large to avoid source confusion. Thus the flux density uncertainties due to source confusion will be significant. To definitively distinguish between extinction and stellar age effects, we will need to await the start of ALMA which can detect the thermally reprocessed far-infrared emission from these objects. Spectroscopy with ALMA will also measure the ratio between the 158 μm [C II] line and $L_{\rm IR}$ in these objects which can be used to discriminate between brief mergers and temporally extended cold-flow

[11] http://jwstetc.stsci.edu/etc/input/nirspec/spectroscopic/

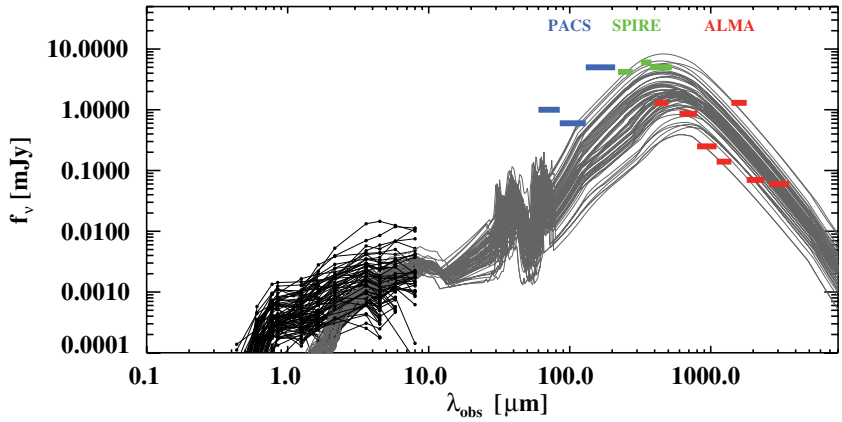

Figure 13. Infrared galaxy templates that represent $L_{\rm IR}$ for each object at its corresponding redshift. The templates are drawn from Chary & Pope (2010). The observed photometry data points from B band to IRAC 8.0 μm is overplotted with small filled circles and the connected lines. The thick horizontal color bars are limits for current and future surveys at longer wavelengths. The blue bar represent *Herschel*/PACS, the green bar shows *Herschel*/SPIRE limits in the GOODS-Herschel observations, and the red bar shows the expected ALMA limits. ALMA limits indicate the expected continuum sensitivities obtained with 60 s exposure, at 12 m array configuration. The majority of these objects are beyond the sensitivity of current far-infrared instrumentation. ALMA will be required to assess if the observed strong Hα emission relative to the UV continuum is a result of dust obscuration.

(A color version of this figure is available in the online journal.)

driven star formation. The former scenario would show ratios that are almost an order of magnitude lower than the latter.

7. SUMMARY

We have studied the multiwavelength properties of a sample of 74 galaxies that have spectroscopic redshifts in the range $3.8 < z < 5.0$ over 330 arcmin^2 of the GOODS-North and GOODS-South fields. The stellar continuum of these objects is well determined through SED fits to the multi-band photometry from the optical to the MIR ($B, V, i, z, F110W, F160W, J, H, K$, 3.6 μm, 4.5 μm, 5.8 μm, and 8.0 μm). Their stellar population ages, star formation histories, extinction laws, $E(B-V)$, and stellar masses are determined through this SED fitting. We demonstrate that the majority of galaxies show excess in the IRAC 3.6 μm band relative to the expected stellar continuum, which is likely due to the redshifted Hα emission line. We define the significance factor S of the 3.6 μm excess compared to the average SED fitting residuals in other filters and used this factor to select Hα emitting galaxies. HAEs are defined as galaxies with $S_{3.6\,\mu\rm m} > 10$. The HAE selection using this excess in a broadband filter identifies galaxies with large Hα EWs and high SFR. The rest-frame EW ranges between 140 and 1700 Å, while SFRs are in the range between 20 and 500 $M_\odot$ yr^{-1}. The derived Hα line luminosity ranges between 2.5×10^{42} erg s^{-1} and 6.3×10^{43} erg s^{-1}. The z$\sim$4 galaxy population appears to show a factor of $\sim$2–3 stronger Hα emission than $z \sim 1$ and $z \sim 2$ galaxies.

The factors that affect Hα emission include: dust extinction, stellar population age, star formation history, IMF, and galaxy metallicity. The flux ratio $F_{\rm H\alpha}/F_{\rm UV}$ is an extinction indicator independent of UV spectral slope β. The relationship between β and $F_{\rm H\alpha}/F_{\rm UV}$ depends on the form of the dust extinction law, with $F_{\rm H\alpha}/F_{\rm UV}$ ratio being higher for the SMC extinction law than for the starburst extinction law when the UV slope β is fixed. The large Hα fluxes and large $F_{\rm H\alpha}/F_{\rm UV}$ ratio of $z \sim 4$ HAEs imply that $z \sim 4$ HAE galaxies prefer the SMC extinction law rather than the SB extinction law. A lower metallicity stellar population and a more top-heavy IMF compared to lower redshift (e.g., $z \sim 2$) galaxies are expected to be another possible reason for strong Hα emission. However, the most dominant driver for strong Hα emission appears to be the temporally extended star formation history of these HAEs based on their location in the stellar age versus EW(Hα) phase space.

At least 60% of HAEs are classified as continuously star-forming galaxies suggesting that this phase is more common than the bursty, short-duration star formation that occurs through mergers. If the HAEs continue to form stars constantly with the observed SFR, HAEs would evolve into massive galaxies ($>10^{11} M_\odot$) at $z \sim$ 2–3. While the number density of $z \sim 4$ SMGs discovered to date is not sufficient to explain the number density of massive galaxies at $z \sim$ 2–3, HAEs can account for $\gtrsim$50% of the stellar mass density in massive galaxies at $z \sim$ 2–3 indicating that the strong Hα phase plays a dominant role in the growth of galaxies at high redshift. We believe that these luminous HAEs are ideal targets for future observations with *JWST*, which would enable their Hα emission to be spectroscopically confirmed, and with ALMA which would place strong constraints on the nature of dust extinction as well as the dominant physical mechanism powering star formation at $z > 4$.

We thank the entire GOODS team for their effort in compiling and reducing different components of the data. We thank Rychard Bouwens and Avishai Dekel for helpful comments and discussions and the anonymous referee for a thorough referee report. This work is based, in part, on observations made with the *Spitzer Space Telescope*, which is operated by the Jet Propulsion Laboratory, California Institute of Technology under a contract with NASA. Part of the NIR data are based on observations obtained with WIRCam, a joint project of CFHT, Taiwan, Korea, Canada, France, at the Canada–France–Hawaii Telescope (CFHT) which is operated by the National Research Council (NRC) of Canada, the Institute National des Sciences de l'Univers of the Centre National de la Recherche Scientifique of France, and the University of Hawaii.

REFERENCES

Adelberger, K. L., & Steidel, C. C. 2000, ApJ, 544, 218
Alexander, D. M., Bauer, F. E., Brandt, W. N., et al. 2003, AJ, 126, 539
Ando, M., Ohta, K., Iwata, I., et al. 2004, ApJ, 610, 635
Atek, H., Malkan, M., McCarthy, P., et al. 2010, ApJ, 723, 104
Bertin, E. 2006, ASP Conf. Ser. 351, Astronomical Data Analysis Software and Systems XV, ed. C. Gabriel et al. (San Francisco, CA: ASP), 112

Bertin, E., & Arnouts, S. 1996, A&AS, 117, 393
Bertin, E., Mellier, Y., Radovich, M., et al. 2002, ASP Conf. Proc. 281, Astronomical Data Analysis Software and Systems XI, ed. D. A. Bohlender et al. (San Francisco, CA: ASP), 228
Bouwens, R. J., Illingworth, G. D., Franx, M., & Ford, H. 2007, ApJ, 670, 928
Bouwens, R. J., Illingworth, G. D., Franx, M., et al. 2009, ApJ, 705, 936
Bouwens, R. J., Illingworth, G. D., Oesch, P. A., et al. 2010, ApJ, 708, L69
Brandt, W. N., Alexander, D. M., Bauer, F. E., & Vignali, C. 2006, Physics of Active Galactic Nuclei at all Scales, ed. D. Alloin et al., Lecture Notes in Physics, Vol. 693, 185
Bruzual, G. 2007, in ASP Conf. Ser. 374, From Stars to Galaxies: Building the Pieces to Build Up the Universe, ed. A. Vallenari et al. (San Francisco, CA: ASP), 303
Calzetti, D. 2001, New Astron. Rev., 45, 601
Calzetti, D., Armus, L., Bohlin, R. C., et al. 2000, ApJ, 533, 682
Capak, P., Carilli, C. L., Lee, N., et al. 2008, ApJ, 681, L53
Carilli, C. L., Lee, N, Capak, P., et al. 2008, ApJ, 689, 883
Chary, R.-R., & Pope, A. 2010, arXiv:1003.1731
Chary, R.-R., Stern, D., & Eisenhardt, P. 2005, ApJ, 635, L5
Conselice, C. J., & Arnold, J. 2009, MNRAS, 397, 208
Conselice, C. J., Bluck, A. F. L., Buitrago, F., et al. 2011, MNRAS, 413, 80
Coppin, K. E. K., Smail, I., Alexander, D. M., et al. 2009, MNRAS, 395, 1905
Daddi, E., Dickinson, M., Morrison, G., et al. 2007, ApJ, 670, 156
Daddi, E., Dannerbauer, H., Stern, D., et al. 2009, ApJ, 694, 1517
Dekel, A., Birnboim, Y., Engel, G., et al. 2009, Nature, 457, 451
Dickinson, M. 1999, in AIP Conf. Proc. 470, After the Dark Ages: When Galaxies were Young (the Universe at $2 < z < 5$), ed. S. Holt & E. Smith (Melville, NY: AIP), 122
Dickinson, M., Papovich, C., Ferguson, H. C., & Budavári, T. 2003, ApJ, 587, 25
Elbaz, D., Daddi, E., Le Borgne, D., et al. 2007, A&A, 468, 33
Erb, D. K., Steidel, C. C., Shapley, A. E., et al. 2006, ApJ, 647, 128
Fitzpatrick, E. L. 1986, AJ, 92, 1068
Gallego, J., Zamorano, J., Rego, M., & Vitores, A. G. 1997, ApJ, 475, 502
Geach, J. E., Smail, I., Best, P. N., et al. 2008, MNRAS, 388, 1473
Giavalisco, M., Ferguson, H. C., Koekemoer, A. M., et al. 2004, ApJ, 600, L93
Hayes, M., Östlin, G., Schaerer, D., et al. 2010, Nature, 464, 562
Kaspi, S., Brandt, W. N., & Schneider, D. P. 2000, AJ, 119, 2031
Kennicutt, R. C. 1998a, ARA&A, 36, 189
Kennicutt, R. C. 1998b, ApJ, 498, 541
Laidler, V. G., Papovich, C, Grogin, N. A., et al. 2007, PASP, 119, 1325
Leitherer, C., & Heckman, T. M. 1995, ApJS, 96, 9
Leitherer, C., Schaerer, D., Goldader, J. D., et al. 1999, ApJS, 123, 3
Luo, B., Bauer, F. E., Brandt, W. N., et al. 2008, ApJS, 179, 19
Madau, P. 1995, ApJ, 441, 18
Malhotra, S., & Rhoads, J. E. 2002, ApJ, 565, L71
Marchesini, D., van Dokkum, P. G., Förster Schreiber, N. M., et al. 2009, ApJ, 701, 1765
McQuade, K., Calzetti, D., & Kinney, A. L. 1995, ApJS, 97, 331
Meurer, G. R., Heckman, T. M., & Calzetti, D. 1999, ApJ, 521, 64
Mouhcine, M., Lewis, I., Jones, B., et al. 2005, MNRAS, 362, 1143
Muzzin, A., van Dokkum, P., Franx, M., et al. 2009, ApJ, 706, L188
Noeske, K. G., Faber, S. M., Weiner, B. J., et al. 2007, ApJ, 660, L47
Ouchi, M., Shimasaku, K., Okamura, S., et al. 2004, ApJ, 611, 660
Papovich, C., Moustakas, L. A., Dickinson, M., et al. 2006, ApJ, 640, 92
Pettini, M., Rix, S. A., Steidel, C. C., et al. 2002, ApJ, 569, 742
Pope, A., & Chary, R. 2010, ApJ, 715, L171
Prévot, M. L., Lequeux, J., Maurice, E., Prévot, L., & Rocca-Volmerange, B. 1984, A&A, 132, 389
Ravindranath, S., Giavalisco, M., Ferguson, H. C., et al. 2006, ApJ, 652, 963
Reddy, N. A., Erb, D. K., Pettini, M., Steidel, C. C., & Shapley, A. E. 2010, ApJ, 712, 1070
Reddy, N. A., Steidel, C. C., Fadda, D., et al. 2006, ApJ, 644, 792
Retzlaff, J., Rosati, P., Dickinson, M., et al. 2010, A&A, 511, 50
Salpeter, E. E. 1955, ApJ, 121, 161
Schaerer, D., & de Barros, S. 2009, A&A, 502, 423
Schinnerer, E., Carilli, C. L., Capak, P., et al. 2008, ApJ, 689, L5
Schmidt, M. 1959, ApJ, 129, 243
Shim, H., Colbert, J., Teplitz, H., et al. 2009, ApJ, 696, 785
Shioya, Y., Taniguchi, Y., Sasaki, S. S., et al. 2009, ApJ, 696, 546
Siana, B., Smail, I., Swinbank, A. M., et al. 2009, ApJ, 698, 1273
Siana, B., Teplitz, H. I., Chary, R.-R., Colbert, J., & Frayer, D. T. 2008, ApJ, 689, 59
Steidel, C. C., Adelberger, K. L., Shapley, A. E., et al. 2003, ApJ, 592, 728
Storchi-Bergmann, T., Kinney, A. L., & Challis, P. 1995, ApJS, 98, 103
Taniguchi, Y., Murayama, T., Scoville, N. Z., et al. 2009, ApJ, 701, 915
Teplitz, H. I., Malkan, M. A., & McLean, I. S. 2004, ApJ, 608, 36
Vanden Berk, D. E., Daniel, E., Richards, G. T., et al. 2001, AJ, 122, 549
Vanzella, E., Cristiani, S., Dickinson, M., et al. 2005, A&A, 434, 53
Vanzella, E., Cristiani, S., Dickinson, M., et al. 2006, A&A, 454, 423
Vanzella, E., Cristiani, S., Dickinson, M., et al. 2008, A&A, 478, 83
Wang, W.-H., Cowie, L. L., Barger, A. J., Keenan, R. C., & Ting, H.-C. 2010, ApJS, 187, 251
Zackrisson, E., Bergvall, N., & Leiter, E. 2008, ApJ, 676, L9